Chapter 5

Manganese mobility during metamorphism: An example from the 2.5 Ga Kuruman-Penge Formation

Jena E Johnson[1], Samuel M. Webb[2], Nic J. Beukes[3], Woodward W. Fischer[1]

[1]Division of Geological and Planetary Sciences, California Institute of Technology, Pasadena, CA 91125, USA. [2]Stanford Synchrotron Radiation Lightsource, Menlo Park CA 94025. [3]University of Johannesburg, Auckland Park, South Africa

ABSTRACT

Manganese-enriched sedimentary rocks from the geologic record are often used as evidence of an oxygenated water column. This inference stems from two important attributes of manganese: 1) manganese concentration in sedimentary rocks requires oxidation and 2) thermodynamics dictates that manganese oxidation demands high redox potential species like oxygen. For massive deposits of manganese dating to after the great rise in oxygen at ca. 2.3 billion years ago, this logic likely holds true. However, there are several ancient examples of manganese-enriched rocks before the emergence of free oxygen, conflicting with the classical proxies for oxygen like redox-sensitive detrital grains and the behavior of iron in paleosols. We probed one such reported manganese enrichment in a highly metamorphosed succession in the Transvaal Supergroup from the South African Kaapvaal Craton (Miyano and Beukes, 1997). These sedimentary rocks date to ca. 2.5 billion years ago, well before the great rise of oxygen, and comprise a craton-wide sequence that has established metamorphic gradients due to contact metamorphism from the 2.05 Ga Bushveld Igneous Complex in the eastern Transvaal basin. We collected core samples across a transect of correlative rocks through a metamorphic gradient from lower

greenschist facies in the west up to amphibolite facies in the east. Examining these samples with whole-rock ICP-MS, X-ray fluorescence and spectroscopic imaging, and electron microscopic analyses including energy dispersive spectrometry and backscatter diffraction, we determined that manganese was primarily in trace levels in authigenic and detrital carbonates, but at higher metamorphic grades manganese had been enriched in and precipitated as manganoan garnets, amphiboles, and a variety of carbonates. Both texture and mineralogical assemblages yield clues to the source, whether depositional or metasomatic, of the manganese. Our results indicate that manganese can and does become enriched in minerals and, occasionally, in whole-rock concentrations during contact metamorphism. However, we cannot distinguish between more local mobilization and Mn concentration from nearby sediments and/or the underlying Archean carbonates, or Mn sourcing from hydrothermal fluids enriched in manganese. Regardless, our well-preserved samples suggest that manganese was not being significantly oxidized and concentrated in western Kaapvaal Craton sediments at 2.5 Ga.

INTRODUCTION

Manganese is a powerful redox proxy to understand ancient environmental redox conditions. Unlike various other redox proxies, manganese has a very high reduction-oxidation potential and thus only certain common environmental oxidants like O_2 or species derived from O_2 like superoxide can chemically oxidize manganese (Stumm and Morgan, 1996; Luther, 2010). When manganese is oxidized, it is deposited in the

sediments and therefore concentrated in the rock record. However, reduced manganese (Mn^{2+}) is soluble and manganese will remain as a reduced cation in anoxic water with its primary sink being a low degree (≤1%) of substitution for Ca in carbonates (Veizer, 1978; Wallmann et al., 2008). Archean carbonates from before the rise of oxygen consequently have high Mn levels of approximately 1% MnO while Phanerozoic carbonates record a very different Mn cycle, averaging 30ppm MnO (Veizer, 1978; Holland, 1984; Komiya et al., 2008). Manganese has the further advantage of being a major component of the environmental system: as the third most abundant transition metal in Earth's crust, the behavior of manganese and in-depth examinations of its mineral hosts are relatively easy to determine by X-ray spectroscopy. These overall abundance, redox, and solubility attributes of manganese make the rock record of Mn especially illuminating to understand paleo-redox constraints.

Indeed, manganese enrichments have been used as evidence for oxygen during the Precambrian Era time and time again. The largest manganese ore deposit, the giant Kalahari manganese field in the 2.2 Ga Hotazel Formation (Gutzmer, 1996), has been linked to the oxygenation of Earth's surface oceans (Kirschvink et al., 2000). Other major manganese ore deposits appear only after the rise of oxygen (Johnson et al., Chapter 1), consistent with oxygen being required to concentrate manganese in sediments, such as the Neoproterozoic Urucum deposit (Urban et al., 1992), the Jurassic Molango deposit (Okita et al., 1988), and the Oligocene Baltic Sea deposits (Varentsov and Grasselly, 1976).

Manganese-enriched rocks from Archean strata before the rise of oxygen have also been noted in India, Brazil, and South Africa, suggesting small amounts of oxygen may be present prior to the rise of oxygen (Roy, 2000; Smith et al., 2010; Planavsky et al., 2014). These manganese-bearing strata include Mn oxides in shale from the ca. 3.1 Ga Iron Ore Group in the Singhbhum Craton in India, Mn oxides and silicate-carbonates in the ca. 2.8-2.6 Ga Khondalite Group in the Indian Eastern Ghats Belt, Mn oxide ore in stromatolitic chert-carbonate of the ca. 2.7-2.6 Ga Chitradurga Group in the Dharwar Craton, Mn oxide beds in limestone in the >2.65Ga Sandur Group of South India, the ca. 2.9-2.7 Ga Jequie Complex in Brazil with Mn silicate-carbonate protolith, and Mn carbonate and garnet in the ca. 2.9 Ga Witwatersrand-Mozaan succession in South Africa (Roy, 2000; Roy, 2006; Smith et al., 2010; Planavsky et al., 2014). All of these rocks are metamorphosed, with some even categorized in the granulite facies (>700degC and 2-15kbar) (Roy, 2000). This metamorphism creates difficulties in assessing what the primary minerals were in some of these deposits. Furthermore, several of these deposits are highly weathered, and may be formed or enriched in Mn from supergene processes in carbonates during dissolution and oxidative weathering (Varentsov, 1996; Roy, 2006). Traditionally, these Indian, Brazilian, and South African deposits have been interpreted as evidence for manganese oxidation by oxygen and thus oxygenic photosynthesis being present far earlier than the rise of oxygen would suggest (Roy, 2006; Smith et al., 2010; Maynard, 2010; Planavsky et al., 2014).

In this study, we investigated less well-known manganese-enriched minerals from the Transvaal Supergroup in the Kaapvaal Craton of South Africa to understand whether they

were environmental signals of manganese oxidation (and by inference, indicating the presence of oxygen or manganese-oxidizing photosynthesis (Johnson et al., 2013)) prior to the major rise of oxygen. Manganese-enriched garnets from ca. 2.5 billion year old sediments were reported from drill cores obtained near the Bushveld Complex, a massive layered suite that intruded into the Transvaal Supergroup (Eriksson et al., 1995; Miyano and Beukes, 1997). The Kaapvaal craton has well-known metamorphic gradients caused by contact metamorphism associated with the Bushveld Complex in the east, and this enabled us to compare manganese concentrations and mineralogical properties in metamorphosed samples from the eastern Kaapvaal to better-preserved samples from the western Kaapvaal (Kaufman, 1996; Miyano and Beukes, 1997; de Kock et al., 2009). This metamorphic gradient also presents an ideal field laboratory to explore the behavior of manganese under different levels of metamorphism. The western strata in the Griqualand West basin is relatively unaffected and categorized as lower greenschist facies (Miyano and Beukes, 1984) but the eastern portion of the Kaapvaal craton (the Transvaal basin) was strongly impacted by the Bushveld intrusion and is greenschist facies reaching amphibolite facies in places (Buick et al., 2001).

GEOLOGIC SETTING

The Neoarchean to Paleoproterozoic lower Transvaal Supergroup in South Africa comprises a well-exposed and well-preserved sequence encompassing the stratigraphy before and after the great rise in oxygen. The Transvaal is recorded in two major basins of the Kaapvaal Craton: the Transvaal basin in the east and the western Griqualand West basin. The Transvaal Supergroup begins with the clastic Wolkberg-Schmidtsdrif

sediments, which are uncomformably overlain by the Black Reef Quartzite grading into the Campbellrand-Malmani carbonate platform rocks (Sumner and Beukes, 2006). This platform was 1.5 to 2 km thick, deepening to the south and west, and then it was drowned around 2.5 billion years ago, recorded in the transitional shales and large iron formation deposition hosted by the contemporaneous Kuruman Formation (Griqualand West) and Penge Formation (Transvaal) (Beukes, 1987; Sumner and Beukes, 2006). Subsequent shoaling is indicated by the shallower-water granular iron formation in the Griquatown Formation overlying the Kuruman Formation in Griqualand West, followed by the mixed siliclastic and iron formation-rich Koegas Subgroup (Beukes and Klein, 1992; Johnson et al., 2014). In the Transvaal basin, the Penge Formation is overlain by the carbonates of the Tongwane Formation prior to an unconformity (Guo et al., 2009).

The strata with reported manganese-enriched garnets lie near the boundary between the Campbellrand-Malmani carbonate platform and the Kuruman-Penge iron formation (Miyano and Beukes, 1997), and thus they are constrained across the craton by several important zircon ages. The Gamohaan formation has been dated at 2521 ± 3 Mya (Sumner and Bowring, 1996) and at 2516 ± 4 Mya (Altermann and Nelson, 1998), and the Riries Member of the Kuruman overlying the Groenwater member is constrained by a U-Pb age of 2460 ± 5 Mya (Pickard, 2003). The 2521 Mya age is from a volcanic ash 40-50m below the contact between the Campbellrand-Malmani Subgroup and the Kuruman-Penge Iron Formation of the Transvaal supergroup (Sumner and Bowring, 1996), which is approximately the beginning of our sampling interval.

The Bushveld Complex of southern Africa introduced a massive layered mafic intrusion into the sediments of the Transvaal Supergroup (Harris et al., 2010). The intrusion occurred at approximately 2.05 Ga (Walraven et al., 1990; Buick et al., 2001). Temperatures of >700°C have been implied by the mineral assemblage in the inner-most zone, which has migmatites, schists, and sillimanite-bearing hornfels (Kaneko and Miyano, 1990). The Bushveld Complex also introduced hydrothermal fluids resulting in major deposits of platinum-group elements, base-metal sulfides, chromites, and vanadium ores (Eriksson et al., 1995; Lee, 1996). Other geochemical and textural studies of the migmatite zone in the Bushveld aureole concluded that there was localized fluid infiltration-driven melting of sandstones, and fluid fluxing caused open-system behavior of at least Ba and Sr during and after melting (Harris et al., 2003). Fluid inclusions from Bushveld Complex granite had daughter crystals with high iron, manganese, chlorine, calcium, sodium, and potassium, suggesting the late Bushveld fluids were enriched in manganese among other elements (Ollila, 1984).

The shales which mark the transition between the carbonate platform and iron formation have been previously reported to host Mn-enriched garnets near the Bushveld complex (Miyano and Beukes, 1997), and this provided a target for our comparison of the manganese phases and abundance throughout the craton. We sampled the same lithologies in cores from the transition between the Campbellrand-Malmani carbonate platform strata and the development of the overlying Kuruman-Penge iron formation, carefully selecting cores adjacent to the Bushveld complex and from the well-preserved rocks to the west (Figure1). The metamorphism-affected cores chosen were drilled at

Penge and Mafefe, where mineralogical assemblages constrain metamorphic pressure at 2.6±0.8 kbar and temperatures of 420-460°C and 340-420°C, respectively (Miyano and Beukes, 1997). This contrasts with mineralogical constraints on the temperatures reached by better-preserved strata in Griqualand West, which are only 110-170°C (Miyano and Beukes, 1984).

MATERIALS AND METHODS

We acquired drill core samples and one sample from a mining pit to assess manganese abundance and mineralogy. We sampled six drill cores, GKP-01, GKF-01, DI-1, WB-98, MF-2, and PA-13, at the South African Council for Geosciences, obtaining several representative carbonate, shale, and iron formation samples from each core across the transition between the carbonate platform strata and the Kuruman-Penge iron formation (Figure 1). Photos of these samples can be found in Figure 2. The majority of the samples were shale and iron formation, but a few representative carbonate and Bushveld-associated sill samples were chosen as well (Figure 2). These strata include the top of the Gamohaan formation, where a clastic shale is developed, to the Kliphuis and lower Groenwater members of the Kuruman Iron Formation (Figure1b) (Beukes, 1984). We also sampled at the Kumba Iron Ore Mine in Thabazimbi (TH, Figure1a), obtaining a ferrunginous shale mining pit sample from near the carbonate-iron formation boundary (Figure 2).

Additional data was obtained on well-preserved core samples from the Kuruman and Griquatown Iron Formations. These samples were examined for comparative purposes by

N. Beukes and are derived from the PAN21 core (Griquatown Formation) and the P4010 core (Kuruman Iron Formation). Bulk Mn wt. % data from these samples were included in Table 1 and Kuruman data was used for comparison purposes as a well-preserved endmember example, in conjunction with results from Schroder et al (2006).

We chose representative shale, iron formation, and carbonate samples to measure manganese concentration, in both a bulk-powder form and by mapping manganese abundance across a thick section. Bulk powders from all cores were evaluated at the Activation Labs in Ancaster, Ontario. Using a lithium metaborate/tetraborate fusion-ICP method, approximately 0.5g of rock were pulverized and mixed with lithium metaborate and lithium tetraborate. A 5% nitric acid solution with an internal standard was added to the molten sample melt, and this was mixed approximately 30 min until completely dissolved. Manganese concentration was determined using a combination/simultaneous Thermo Jarrell-Ash ENVIRO II ICP or a sequential Varian Vista 735 ICP. The samples were run with replicates, a method reagent blank and certified reference material, and the instrument is calibrated using seven certified reference materials. The detection limit is 0.001% and accuracy determined from standards is 2.3% or better for MnO > 0.1 wt. % and about 12% for MnO < 0.1 wt. %.

Manganese concentration maps across thick sections of core and mine samples were produced using a mesoprobe X-ray beam rastered across the sections at the Stanford Synchrotron Radiation Lightsource using beam line 10-2. The beam was ~30μm, pixels were designated at ~50μm x 50μm, and we used a Vortex SII International Silicon drift

detector to collect manganese X-ray fluorescence. The incoming beam energy was set at 13,500 eV to excite and measure the fluorescence of other elements in addition to manganese including nickel, iron, and calcium. Iron was often extremely enriched in the ferruginous shales and iron formations, causing iron photons to enter the manganese fluorescence window. We removed most of the iron contribution and isolated the manganese signal using a best-fit polynomial in a Mn v. Fe plot, which usually was Mn = $5x10^{-6}(Fe)^2 + 0.0159(Fe)$. The resultant manganese fluorescence maps enabled us to choose areas from each core to make into thin sections. Some sections were chosen to be representative shales from each location, choosing regions that looked typical of the shale thick section(s) available from an individual core. Other samples were made into thin sections with notably higher localizations of manganese, like the manganese-enriched portion of MF402 and a sample of the higher-manganese particles that appeared in PA1470. These samples were made into microprobe quality thin sections by High Mesa Petrographics and observed optically on a Leica polarizing microscope.

We examined these sample targets using X-ray spectroscopic imaging, a technique that pairs microscale X-ray spectroscopy with microscale X-ray fluorescence mapping to create speciation maps of a designated element (Johnson et al., in review; Mayhew et al., 2011; Johnson et al., 2013). We used beam line 2-3 at the Stanford Synchrotron Radiation Lightsource to measure the manganese X-ray fluorescence at 2-10μm pixels at four specified incoming X-ray energies. A high beam resolution of ~2μm beam size was accomplished using Kirkpatrick Baez focusing mirrors, and a Vortex SII International Silicon drift detector collected the fluorescence signal. We chose energies using

differences in X-ray spectra to best distinguish between various manganese(II),(III), and (IV) phases: 6551eV, 6556eV, 6562eV, and 6590eV. Principal component analyses (PCA) of these four energy maps highlighted areas with differing manganese signals, and helped guide where we measured X-ray absorption near edge structure (XANES) spectra to confirm phase differences. These internal XANES spectra became sample endmembers employed to perform a linear fit using the normalized fluorescence at each energy for every pixel. This best-fitting created manganese speciation maps for each sample. A 2-point averaging was applied to smooth the spectra so noise in the spectra did not affect XANES multiple energy fitting.

The regions of interest chosen for each representative sample were then further investigated on a nano-scale using electron microscopy. We probed textural relationships between minerals using carbon-coated samples (coated with 7-15nm of graphite using a Cressington Carbon Coater) on the scanning electron microscope (SEM) housed in the Caltech GPS Analytical Facility. This SEM is a Zeiss 1550VP Field Emission SEM equipped with an Oxford INCA Energy 300 X-ray Energy Dispersive Spectrometer (EDS) system and an Electron Backscatter Diffraction (EBSD) system. We captured high-resolution images in backscatter mode, enhancing compositional contrast, and identified minerals using elemental and diffraction analyses. Samples for EBSD measurements were additionally polished using a Vibromet 2 vibratory polisher. Quantitative elemental analyses of points have a relative accuracy of better than 5%.

RESULTS

Whole-rock measurements of manganese concentration by fusion-ICP indicated that manganese was not enriched in well-preserved samples from Griqualand West, and only became significantly enriched in one metamorphosed sample. Rock powders relatively unaffected by the Bushveld intrusion-related metamorphism had MnO weight percents ranging from 0.03 to 0.48% in shales and 0.84 to 1% in carbonates (Table 1). A previous study had measured MnO weight percent in the Kuruman iron formation in the well-preserved cores GKF-01 and GKP-01 and the data ranged from 0.07 to 0.33%, averaging 0.18% (Schröder, 2006). Our measurements of whole-rock samples from metamorphosed cores and one mining pit sample reached up to 1.5% MnO in one shale sample, although other shale samples had 0.04 to 0.17% (Table 1). Only the PA2014m sample has significantly enriched manganese, distinguished from the average well-preserved shales with a z-score of 7.16 and a p value of $1*10^{-12}$ ($p << 0.05$, the usual cut-off for significant difference in population). Metamorphosed iron formation showed a very slight enrichment in Mn, with MF402m at 0.68 % Mn having a statistically significant Mn enrichment but close to being within the well-preserved population ($p = 0.035$) and PA1470m 0.57% falling within the normal distribution of the well-preserved iron formation samples ($p = 0.12$). Two carbonates forming the base of the PA-13 core were relatively depleted in Mn, having only 0.025 and 0.039 wt% MnO (Table 1). This is low compared to our measurements of Mn in carbonates (0.8 to 1%), but according to previous measurements of the Campbellrand carbonates in GKP-01 and GKF-01, all of these values do fall within the normal population of these carbonates ($p > 0.05$), which average to 0.19 wt % (Schröder, 2006).

Spatially, our X-ray mesoprobe results revealed that manganese in metamorphosed samples have interesting differences from their well-preserved counterparts (Figure 3). Metamorphosed samples from the Bushveld complex region have abundant grunerite, a fibrous iron amphibole (Miyano and Beukes, 1997). Grunerite seems to have grown during metamorphism with a small but significant amount of manganese, which maps as long fibers or fibrous rosettes in thick section fluorescence maps (Figure3, MF402, PA1355). We could also see discrete Mn-rich areas in some of the metamorphosed sections (Figure3, PA1470, PA2014) that warranted further investigation, and a strong correlation between Ca and Mn. One Bushveld-affected section, MF493, had clear Mn-enriched veins cutting across lamination and that section was also chosen for further analyses. Lower-grade metamorphic sections unaffected by the Bushveld complex were all internally quite similar: Mn was generally very low and associated with Ca in carbonates if enriched at all.

We chose shale samples from each core, targeting areas shown by our mesoprobe to have at least a small amount of Mn in representative samples and those with especially interesting manganese trends, to perform microscale analyses on using X-ray spectroscopic imaging methods and electron microscopy techniques. Initial imaging was performed on an optical microscope, using reflected, transmitted, and polarized light (Figure 4). These paired approaches yielded illuminating results. Many metamorphosed samples had fibrous or blocky Mn-bearing grunerite, an iron silicate in the amphibole group. This identification was confirmed using EBSD, which confirmed that the iron-rich silicate was in the cummingtonite-grunerite family. Manganese and magnesium, and

occasionally calcium, appeared to substitute for iron in grunerite [grunerite formula: $Fe_7Si_8O_{22}(OH_2]$. Since there is no color-based optical evidence of Fe(II)-(III) intervalence transfer or Mn(III) presence (the grunerite is white, Figure4), we agree with Klein, who also asserted that the grunerite was all Fe(II) (Klein, 1968). The likelihood of Mn(III) being present is very low if there is no Fe(III). This is pertinent to the XANES spectra produced from these grunerite samples. Despite having very similar EDS and EBSD spectra, the grunerite has very variable X-ray absorption spectra, including some peaks shifted to higher energy suggestive of an Mn(III) presence (Figure5). We instead propose that these X-ray spectral variations are due to Mn site occupancy differences and/or crystal orientation differences.

Intriguingly, the manganese contents of the grunerite were fairly different sample-to-sample, although intra-sample variations were minor. The widest range of MnO content was found in the most manganese-enriched sample, PA 2014m. Here Mn varied from 1.49 to 6.44 wt. % MnO, although most samples were ~1.9% MnO (Supp Table 1). MF402 had fairly consistent MnO content of its grunerites, ranging from 0.94 to 1.28 and averaging 1.12 wt %. One other sample we examined in depth was PA1470m, and this had only trace levels of Mn, ranging 0.5 to 0.84%, and averaging 0.65 wt. % MnO (Supp Table 1).

Another common manganese mineral host was carbonate phases, from manganoan calcites and dolomites to manganese-enriched siderites and rhodochrosites. Well-preserved shales and carbonates had low levels of manganese (up to ~1 atomic % Mn,

averaging 0.5%) as well as iron (~2.6% Fe) incorporated into calcites and dolomites. These carbonates were either ~10-30um euhedral crystals or detrital carbonate grains, except for a highly recrystallized section from D1-1 (218m) which exhibits exsolution of a mixed cation carbonate into calcite and manganoan and ferruginous pseudo-dolomite (~30% of cations were Mg). The temperatures predicted by the Mg content of the calcites range from 250-330ºC (Goldsmith and Newton, 1969) (Supp Table 1), considerably higher than the regional diagensis predicted by other methods (Miyano and Beukes, 1984). Therefore, the exsolution into two endmember phases was likely incomplete and had not yet reached equilibrium. Metamorphosed thin sections from PA-13 and MF-2 also had manganoan carbonates: samples MF402, PA1470 and PA2014 had ferruginous (~7-20 atomic % Fe) carbonates with ~0.5-2.5 atomic % Mn and MF493 had manganoan siderites and even rhodochrosite in veins with 6-17 atomic % Mn. Other than the higher iron content (~7-20 atomic % Fe), the textures of the carbonates also contrasted with the well-preserved samples.

The presence and distribution of manganoan grunerite, carbonate, and other minerals were distinct for each sample we explored in-depth. Figure 5 shows PA2014, a black shale that now has abundant porphyroblasts of manganoan almandine garnet, with about 9% Fe, 4.5% Mn, and 2.8% Ca (Supp Table1). It also has iron sulfides, likely pyrite, and manganese-bearing and fibrous grunerite veins with a small amount of grunerite dispersed throughout the matrix that cross-cuts lamination (Figure 5). In a background of iron (± K, Mg) aluminosilicates and silica, our X-ray spectroscopic imaging picked out four phases hosting manganese (Figure 5). Two of these were ascertained to both be

grunerite, from identical EBSD and EDS signatures. Here we hypothesize that these different grunerite signatures are correlated to the stark crystal orientation differences in the late-stage veins: the grunerite spectral signature corresponds to where SEM imaging shows a clear difference in fiber orientation (Figure 5). This is consistent with other studies which have found dramatic differences in Fe XANES spectra from different crystal orientations (Dyar et al., 2002). The other two manganese-containing minerals were from carbonates and garnets. Carbonates in PA2014 had relatively high manganese, ranging from 1.7 to 2.7% Mn. These were also distinct from well-preserved samples by being highly iron-enriched, averaging 7% iron with ~17% Ca and ~3.5% Mg. Carbonates in PA 2014m were also relatively coarse-grained, comprising crystallites from 30um to >60um (Figure 5).

Aside from the garnets, PA 2014 is similar to two other metamorphosed samples, PA 1470 and MF 402. Both of these sections also had abundant grunerite and manganoan carbonates. MF 402 appears to be almost entirely replaced by grunerite fibers and blocky crystals, although it also has a vein of microcrystalline quartz cemented by large equant carbonate crystals which are manganese-bearing (Figure 6). The carbonate cement has ~1-1.5% Mn and, like PA 2014, very high iron content in the range of 8-9%. PA1470 had large euhedral magnetites rather than garnets, and a matrix of fine manganoan grunerite fibers and silica with aggregates of manganoan carbonate crystals (Figure 7). The grunerite appears to have grown over pre-existing quartz with a few later coarse grunerite fibers, with the coarse magnetite crystals and manganoan calcite cross-cutting the grunerite (Figure 7). The carbonates from PA1470 were, like other metamorphic

carbonates, between calcites and ankerites with ~10% Fe and 16% Ca with minor Mn (~1.2%) and Mg (~3.1%). Small domains appear darker in backscatter images (Figure-) and these were much more Ca-enriched than the majority of the carbonates. The carbonate crystals formed large aggregates often hundreds of microns in both dimensions (Figure 7).

Another metamorphosed shale sample has manganese-enriched mineralized veins, which are often a good sampling of the fluid composition that percolated through the rocks during late diagenesis and metamorphism. MF493 is mostly composed of fine-grained iron, sodium, and potassium aluminosilicates, but it has several large veins cutting through this matrix with high enrichments of sulfides, manganoan siderites, and ferrous rhodochrosites (Figure 8). These carbonates have 6-17 atomic % manganese, the highest Mn concentrations we observed in any sample. The veins also have abundant zinc and iron sulfides, which is consistent with the Zn-Pb mineralization associated with the Bushveld intrusion (de Kock et al., 2009). The co-occurrence of manganese-iron carbonates with zinc sulfides suggests manganese-enriched fluids were sourced from the Bushveld Complex into these rocks. Other nickel-rich iron sulfides (with 3-4 atomic % Ni) are scattered throughout the matrix.

PA 886m does not have nearly as high of manganese content, but its manganese is in an unusual form: large manganese-bearing ilmenite grains that appear detrital in a matrix of iron and magnesium aluminosilicates, quartz, and potassium feldspar (Supp Figure1).

While not a significant source of manganese to the bulk rock (which had only 0.05% MnO), these grains individually reach up to 1.1 atomic % Mn.

Well-preserved shale and carbonate examples were more consistent and only had manganese in trace amounts occurring in carbonates. DI-218 has calcites and ferruginous pseudo-dolomites with small amounts of Mn, with these two phases separated by what appears to be severe recrystallization and exsolution (Figure 9). It also has scattered small iron sulfides. WB 830m has scattered blocky crystals of calcites that have up to ~0.5% Mn in a matrix of potassium aluminosilicates, quartz, and bright block of iron and magnesium aluminosilicates (Figure 10). Some of these carbonates are cored by Mg-rich calcites without much iron or manganese, suggesting that much of the carbonate are overgrowths and cements precipitating during early diagenesis (Figure 10). GKF 338m has abundant calcite as euhedral Mg-enriched cements with small amounts of Fe and trace Mn, alongside potassium aluminosilicates, iron clays, and quartz (Figure 11). GKP 242m is mainly extremely fine-grained K aluminosilicates with rarer iron aluminosilicates and rounded detrital carbonate grains with trace Mn in coarser-grained bands (Figure 12).

DISCUSSION

We examined an array of shale, carbonate, and iron formation samples from the Campbellrand-Malmani carbonate platform to Kuruman-Penge iron formation boundary

to try to understand if manganese was enriched in these sediments through environmental reactions or mobilization and/or introduction during metamorphism. We used the Kaapvaal craton as a natural laboratory with its well-known metamorphic gradients and focused on shales from the Transvaal Supergroup, which had reported manganese enrichments near a large igneous intrusion [the Bushveld Complex] (Miyano and Beukes, 1997). Examining core samples on a micro- and nano-scale, we determined that manganese was moderately enriched in carbonates, garnets, and amphiboles in samples from the Transvaal close to the Bushveld Complex but manganese was only a trace component of carbonates in cores from the better-preserved Griqualand West region. Thus manganese was mobilized, enriched, and altered mineralogically, probably related to the contact metamorphism and hydrothermal fluid fluxes associated with the Bushveld Complex.

Manganese enrichment and remineralization implies that manganese was mobilized during the high heat and pressure conditions imposed during metamorphism, but the source of manganese is unclear. We hypothesize three possible explanations for the behavior of manganese that we observe: 1) Manganese was present in the original sediments but locally re-mobilized and concentrated into new minerals during metamorphism; 2) hydrothermal fluids related to the Bushveld Complex were enriched in manganese and thus introduced Mn to the nearby rocks; and 3) the underlying sediments was a source of manganese, potentially the underlying Malmani carbonate undergoing decarboxylation or dissolution, and fluids then brought this Mn up to overlying rocks. Hypothesis #1 we can address with our measurements from the well-preserved correlated

sediments from the other side of the basin. Our observations indicate that manganese was originally in trace amounts in authigenic or detrital carbonates. Many of our metamorphosed sections show manganese in different minerals, like in fibrous grunerite, or in more manganese-enriched carbonates, but the bulk Mn content is similar to their well-preserved counterparts. A couple samples, especially PA2014m but also MF 402m, have higher Mn than we would expect from their better-preserved equivalents. Furthermore, we observed Mn in veins alongside Bushveld-associated minerals like lead sulfides. Both of these observations suggest to us that there was an additional Mn source besides the Mn that could be derived from local sediments, and this source may have been associated with Bushveld fluids.

The other two possible explanations for Mn introduction during metamorphism seem to be both feasible. Late-stage magmatic fluids may contain large quantities of Fe, Mg, and Mn (Burnham, 1979; Kontak and Corey, 1988). In a similar study of manganese-enriched garnet-bearing rocks affected by contact metamorphism by the South Mountain Batholith, magmatic fluids were considered a likely source of Mn (Kontak and Corey, 1988). However, the Mn, Mg, and Fe in hydrothermal fluids were also attributed partially to sourcing from surrounding metasedimentary rocks; it was suggested that some late-magmatic or post-magmatic fluids interacted with the surrounding rocks and extracted and mobilized these elements (Kontak and Corey, 1988). This may have also been true in the Bushveld-associated magmatic fluids. In support of this idea, our measurements of the underlying carbonate in the metamorphosed PA-13 core (Table 1) showed a large (40x) Mn depletion from the better-preserved carbonate examples. However, a more

extensive dataset from well-preserved carbonate samples shows that the metamorphosed carbonates still fall into a normal range for Mn in these carbonates, so this is not necessarily evidence that Mn has been stripped from the underlying rocks.

Regardless of the mobilization mechanism, we can now propose some guidelines for identifying whether manganese in an ancient sedimentary rock was primary or introduced later. Assessing manganese minerals on a micron- to nano-scale greatly helps to show whether manganese-bearing minerals cross-cut other minerals or whether manganese hosts appear to be in expected early phases that do not interrupt other grain boundaries. That said, it is quite difficult to untangle the complexities of ancient rocks, especially metamorphosed strata from Archean time. Ideally, manganese-enriched strata would show expected manganese minerals consistently appearing across kilometers of distance, with trends following expected stratigraphic relationships and unrelated to regional metamorphism.

We can gain from these samples two discrete conclusions: 1) manganese mobility and introduction is a potential problem especially near intrusive igneous complexes, and 2) well-preserved strata at ~2.5 Ga from Griqualand West show no sign of manganese oxidation. Mn-enriched carbonate crystals and mineralized veins, Mn-enriched amphiboles (grunerite), and Mn-enriched garnets from contemporaneous metamorphosed sections and the significance enrichment of at least two samples close to the Bushveld Complex demonstrate that manganese can and does become mobile during metamorphic processes, either by extraction from surrounding strata or from Mn-enriched

hydrothermal fluids. While manganese enrichments were found in 2.5 Ga metamorphosed strata from the Bushveld-affected Transvaal basin, we examined 15 sections (including 4 sections in-depth) from the Griqualand West basin and found no evidence of primary manganese enrichment. This result suggests that manganese was not being oxidized and concentrated in Griqualand West during the ~2.5 Ga transition from carbonate platform to iron formation.

ACKNOWLEDGEMENTS

We would like to thank Bertus Smith for all his time and help with field work in South Africa, Courtney Roach for X-ray microprobe assistance and trouble-shooting, Chi Ma for help with EBSD measurements, and George Rossman for valuable mineralogical consultations and assistance with Raman spectral data collection and interpretation. We also thank John Eiler and Max Lloyd for helpful input. We are also grateful to the Lewis and Clark Foundation for funding field research in South Africa, the Agouron Drilling Project for obtaining GKF and GKP cores, and a Packard Foundation grant to W.W.F. for funding sample analyses. Portions of this research were carried out at the Stanford Synchrotron Radiation Lightsource, a Directorate of SLAC National Accelerator Laboratory and an Office of Science User Facility operated for the US Department of Energy Office of Science by Stanford University.

FIGURES AND TABLES

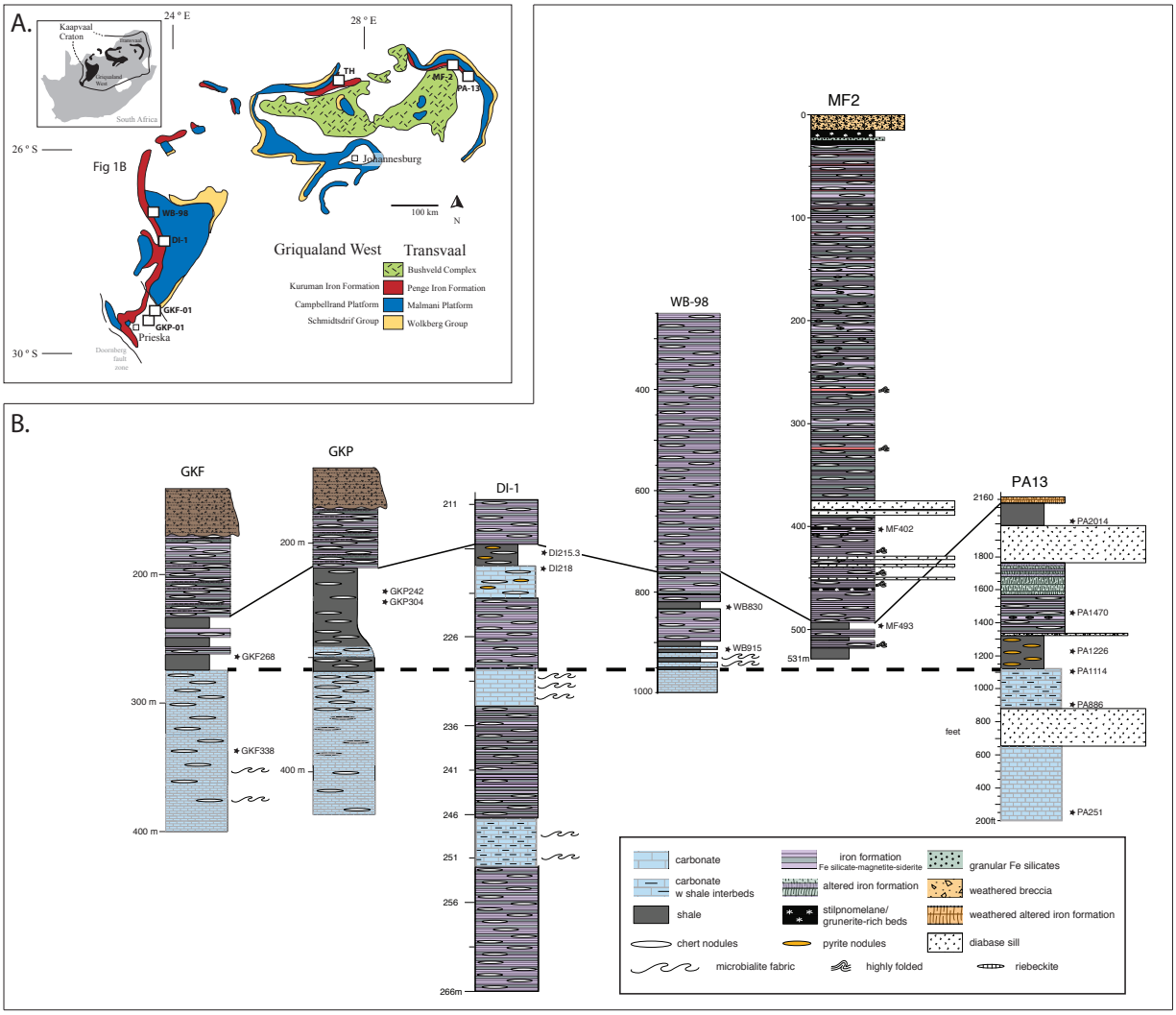

Figure 1 – A. Core locations shown on map of Kaapvaal craton. Inset indicates the location of the Kaapvaal relative to the Republic of South Africa. Well-preserved cores [GKP-01, GKF-01, D1-1, WB-98] are located in the Griqualand West basin. Metamorphosed cores and mining pit sample from Thabazimbi [TH] are derived from the Transvaal basin on the east surrounding the Bushveld Complex (green). B. Core stratigraphy drawn with respect to the legend shown in the lower right. Cores correlated using a lithostratigraphic pseudo datum but could be time-transgressive across platform (Sumner and Beukes, 2006).

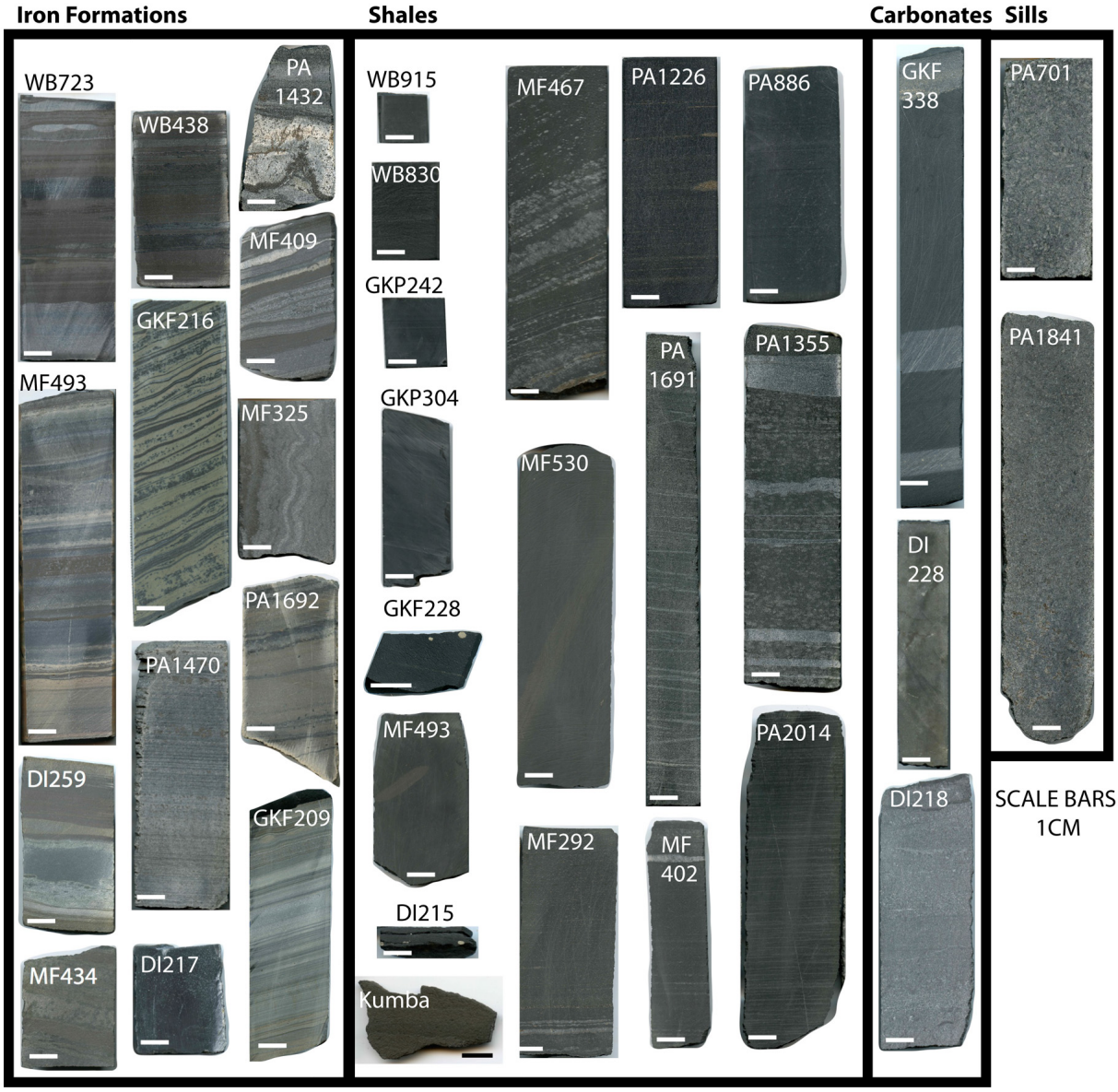

Figure 2 – Photographs of core samples analyzed for Mn content, categorized into shale, iron formation, carbonate, and diabase sill samples as schematically represented in Figure 1.

Figure 3, Panel 1:

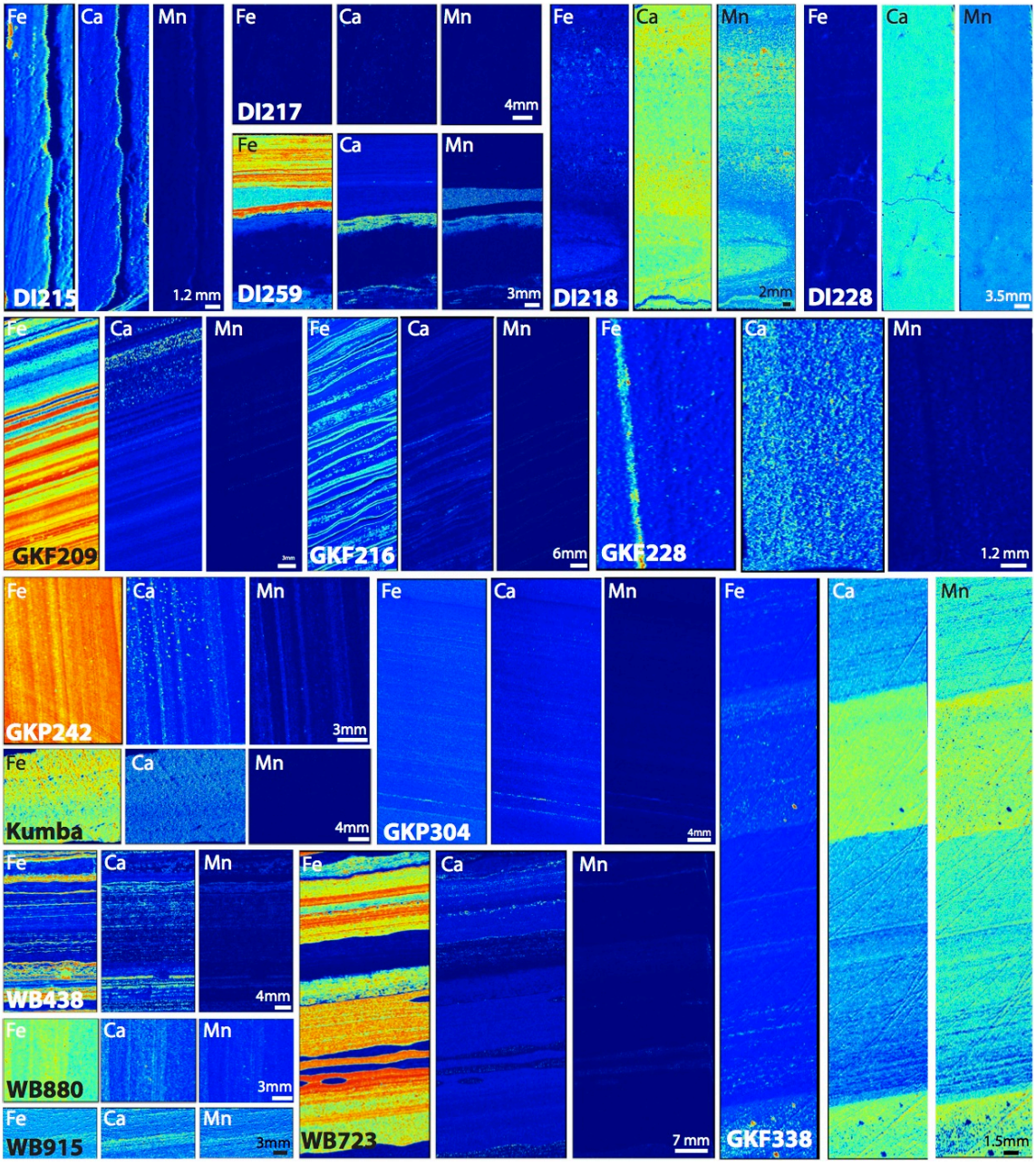

Figure 3, Panel 2:

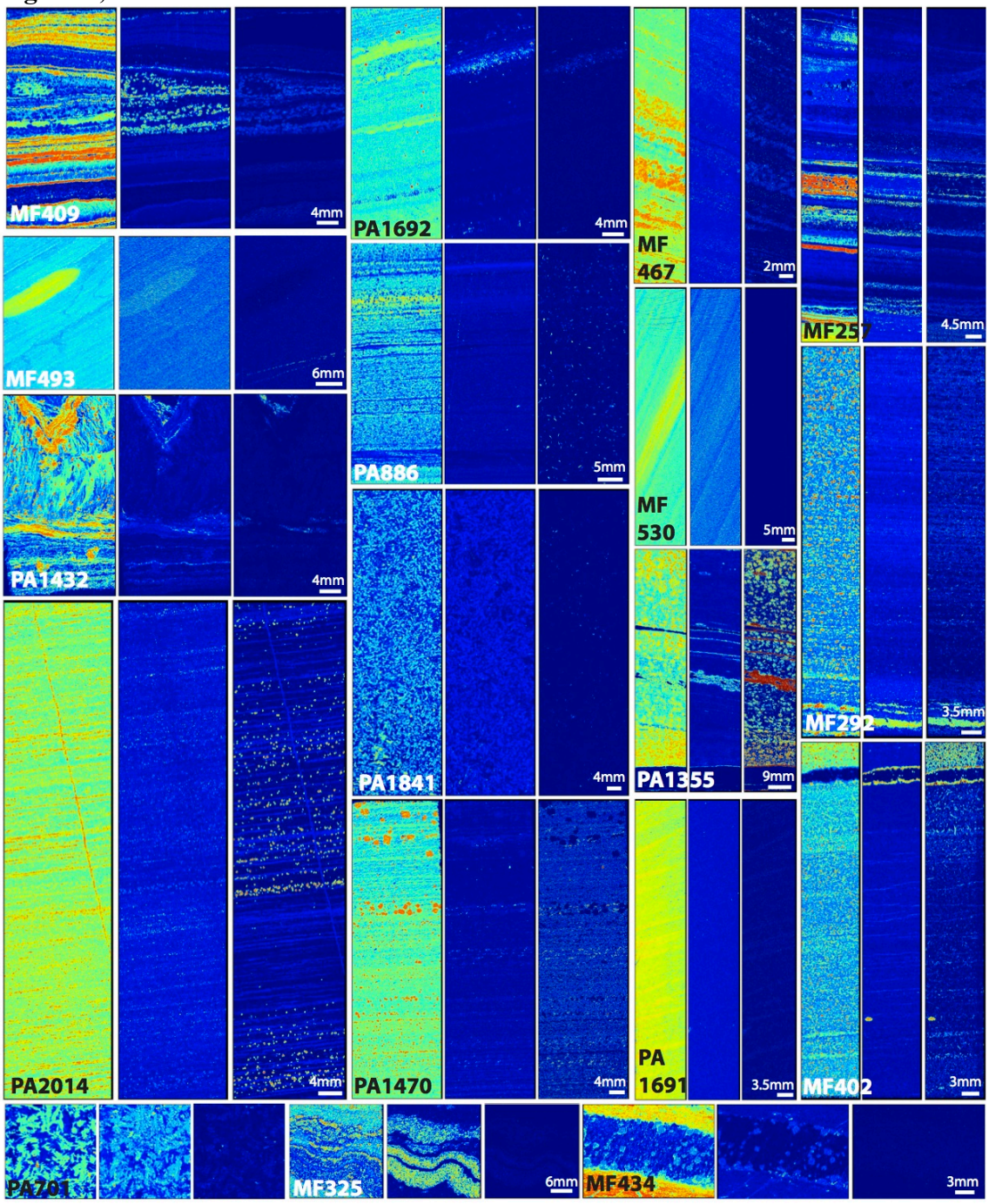

Figure 3 (above) – X-ray fluorescence imaging of iron, calcium and manganese abundance, with all Mn scales set to 100 μg/cm^2 and Fe and Ca set to internal maximums. Manganese data was corrected for iron overlap into the manganese fluorescence window by subtracting the iron contribution into the manganese signal using a best-fit polynomial, fitting the majority of points in a Mn v. Fe plot.

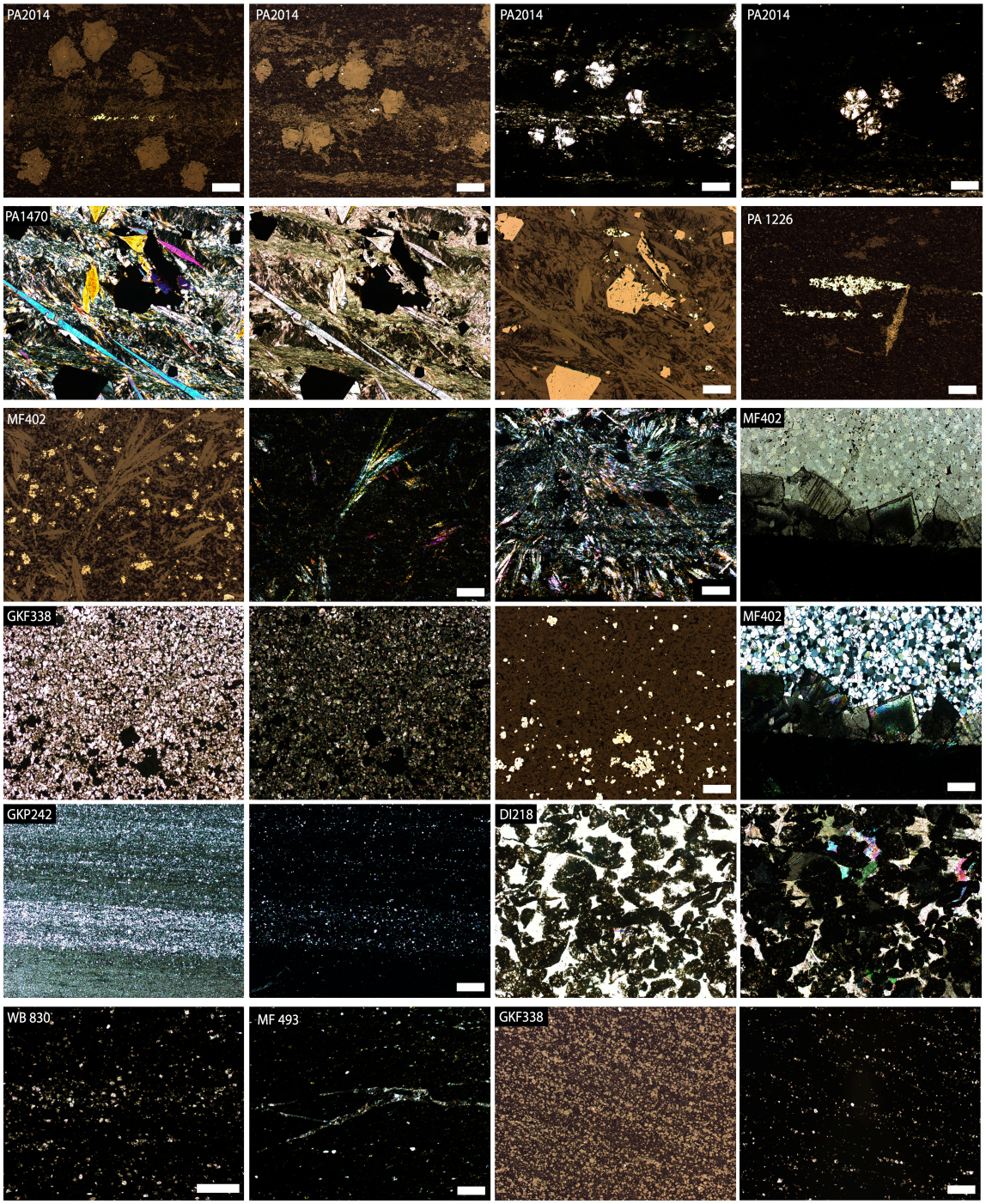

Figure 4 – Microscopic photographs under transmitted, polarized, and reflected light of representative thin section samples from each core. All scale bars are 50µm.

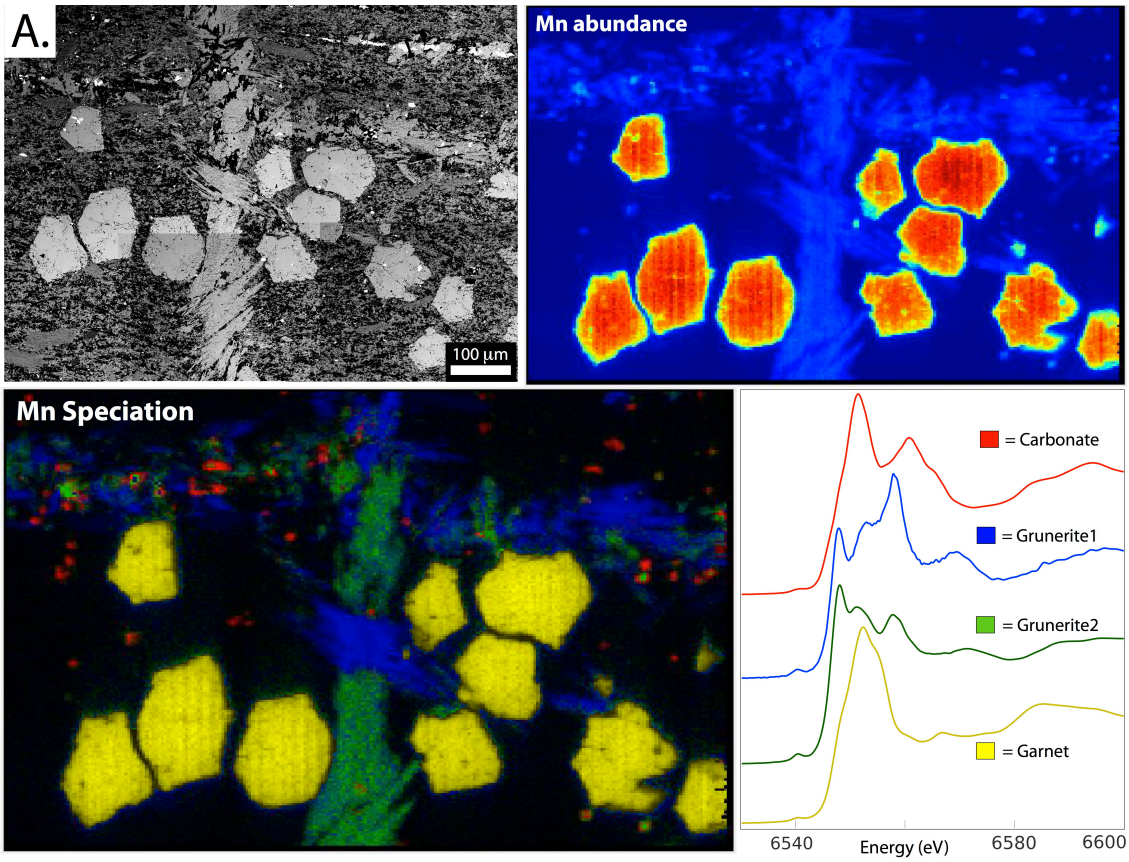

Figure 5 – A. Target region of PA 2014m thin section that had cross-cutting grunerite veins, large garnets, and scattered carbonates. X-ray spectroscopic imaging and spectra are shown on top, imaging garnets (yellow), two types of grunerite (green and blue, see discussion in text), and carbonates (red). B. Scanning electron microscopy images, with mineral identifications made using energy dispersive spectrometry (see Supplementary Table 1).

B.

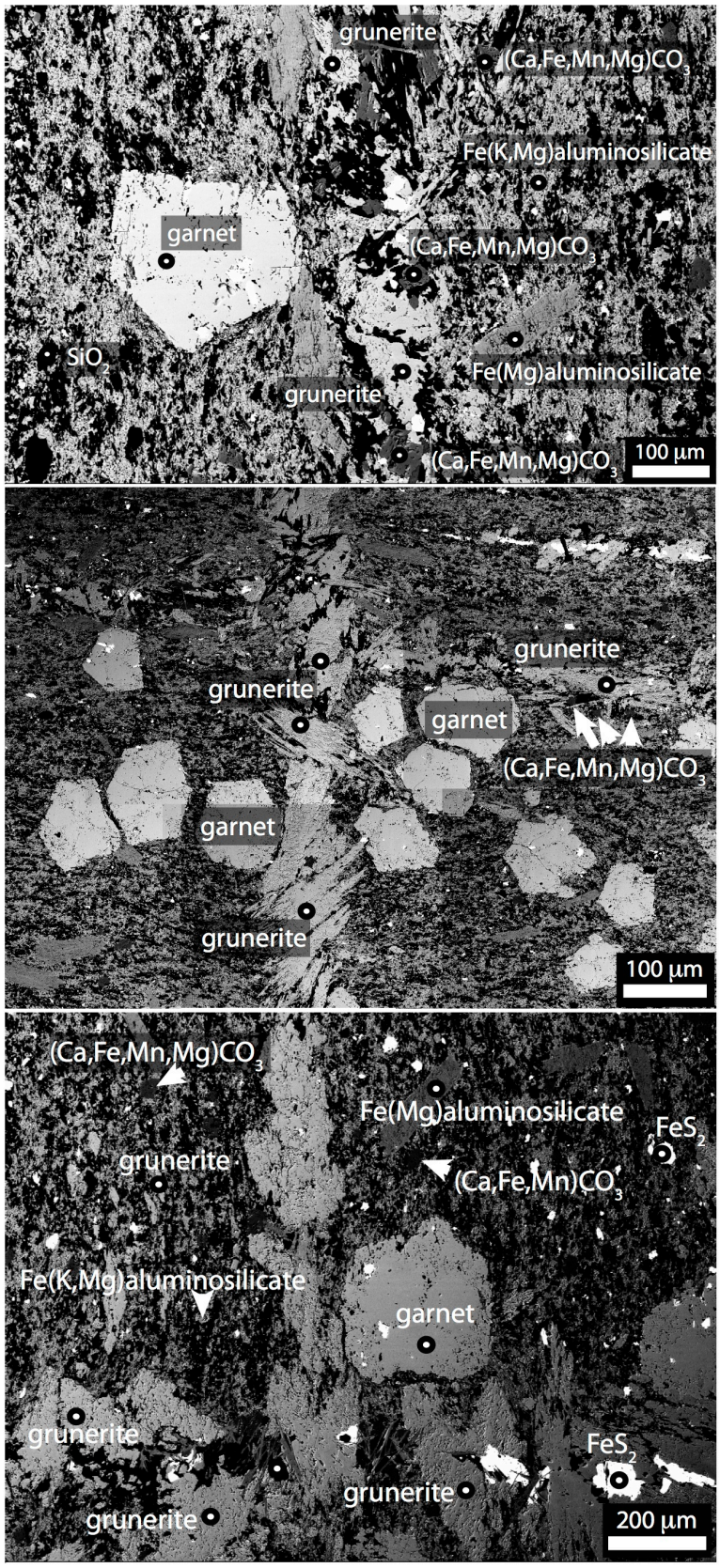
grunerite
(Ca,Fe,Mn,Mg)CO3
Fe(K,Mg)aluminosilicate
garnet
(Ca,Fe,Mn,Mg)CO3
SiO2
Fe(Mg)aluminosilicate
grunerite
(Ca,Fe,Mn,Mg)CO3
100 µm
grunerite
grunerite
garnet
(Ca,Fe,Mn,Mg)CO3
garnet
grunerite
100 µm
(Ca,Fe,Mn,Mg)CO3
Fe(Mg)aluminosilicate
FeS2
grunerite
(Ca,Fe,Mn)CO3
Fe(K,Mg)aluminosilicate
garnet
grunerite
FeS2
grunerite
grunerite
200 µm

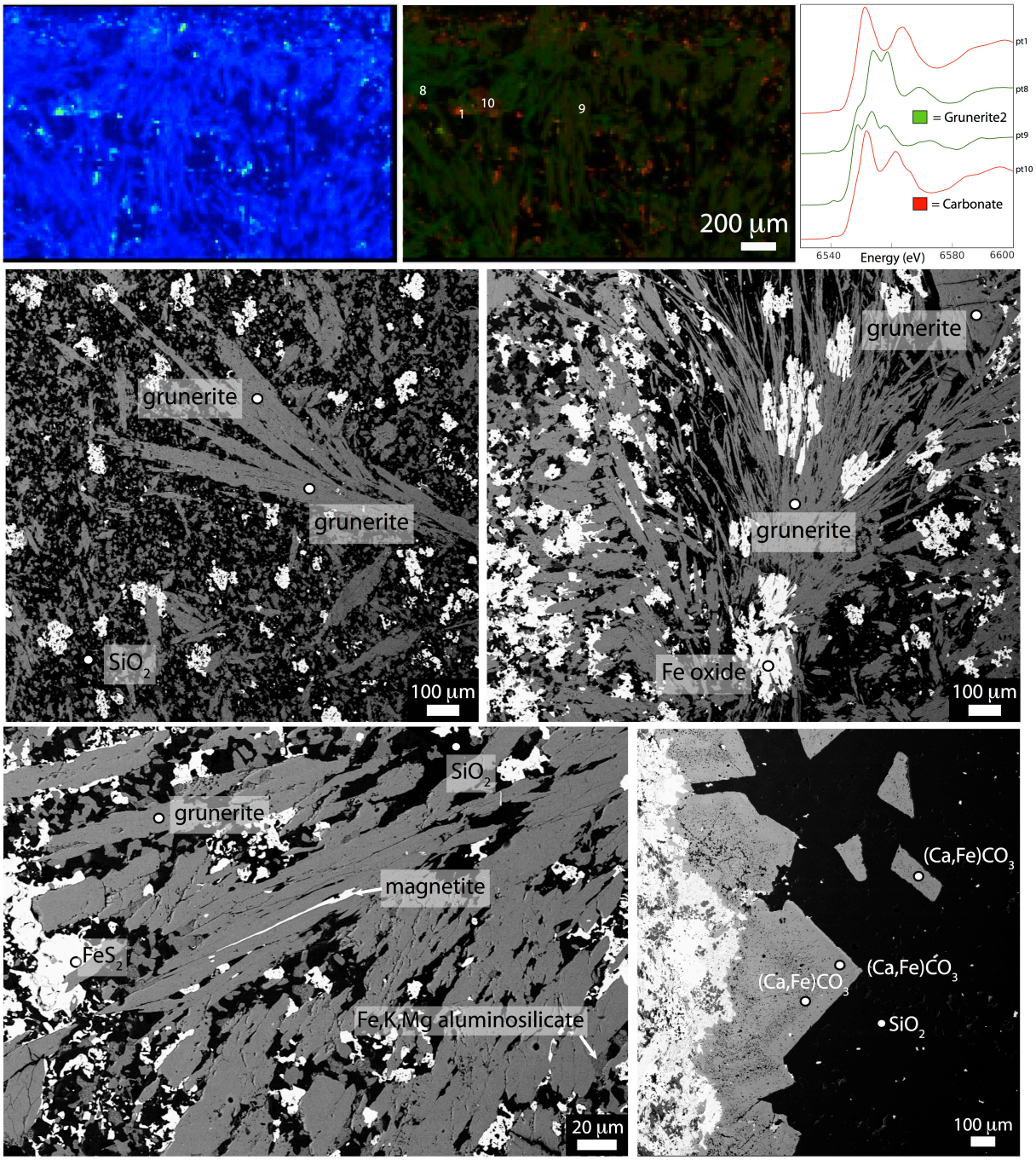

Figure 6 – Representative region of MF 402m with abundant grunerite fibers. Top shows manganese speciation map indicating grunerite (green) and carbonate (red) produced from multiple energy maps and X-ray absorption spectra (top right). SEM photos with mineral identifications shown below for comparison.

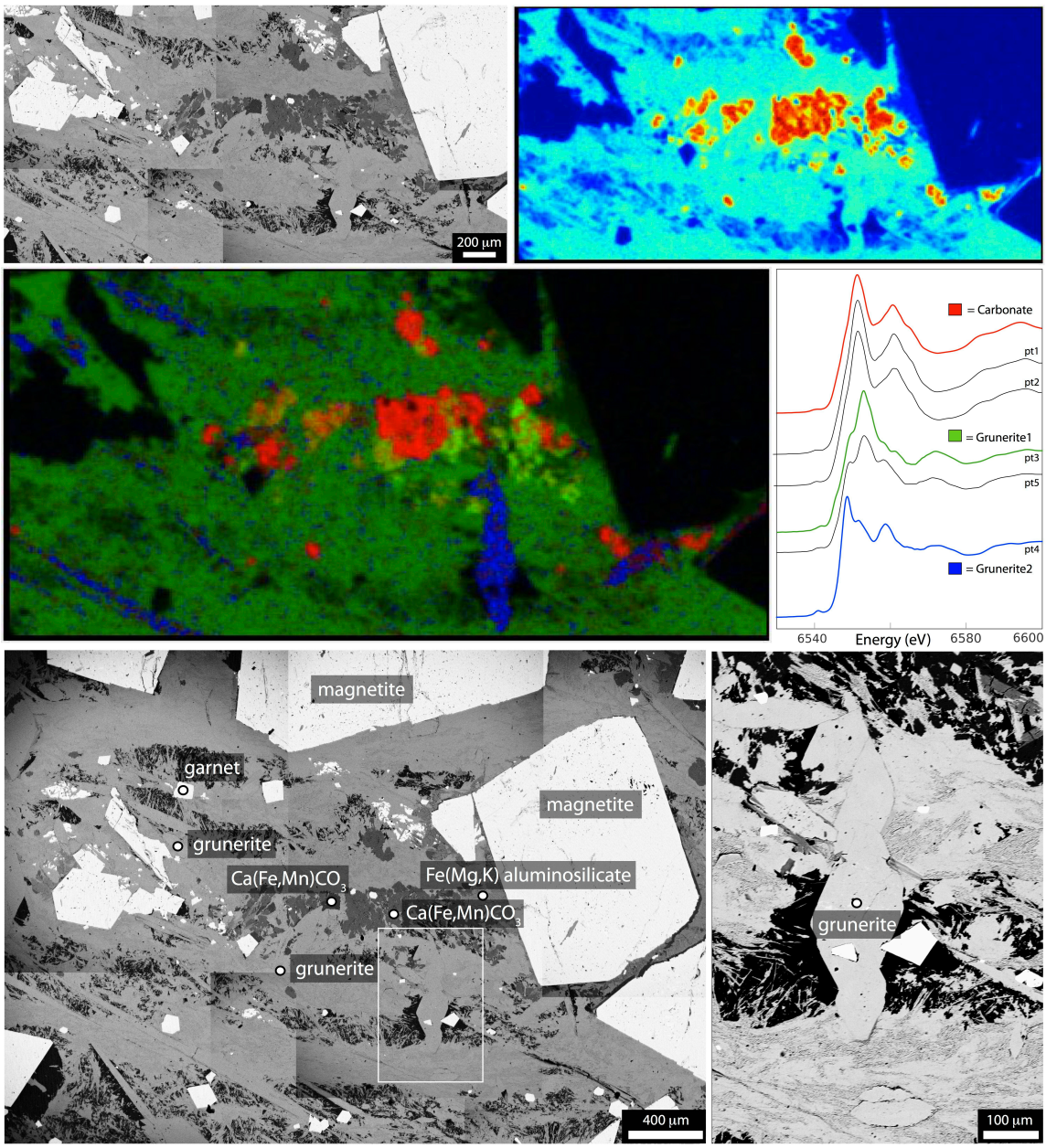

Figure 7 – PA 1470m section focusing on one of the Mn hot spots identified by X-ray fluorescence imaging. The manganese was determined to be hosted by manganoan mixed-cation carbonates, both by X-ray spectroscopic imaging and SEM-EDS analyses.

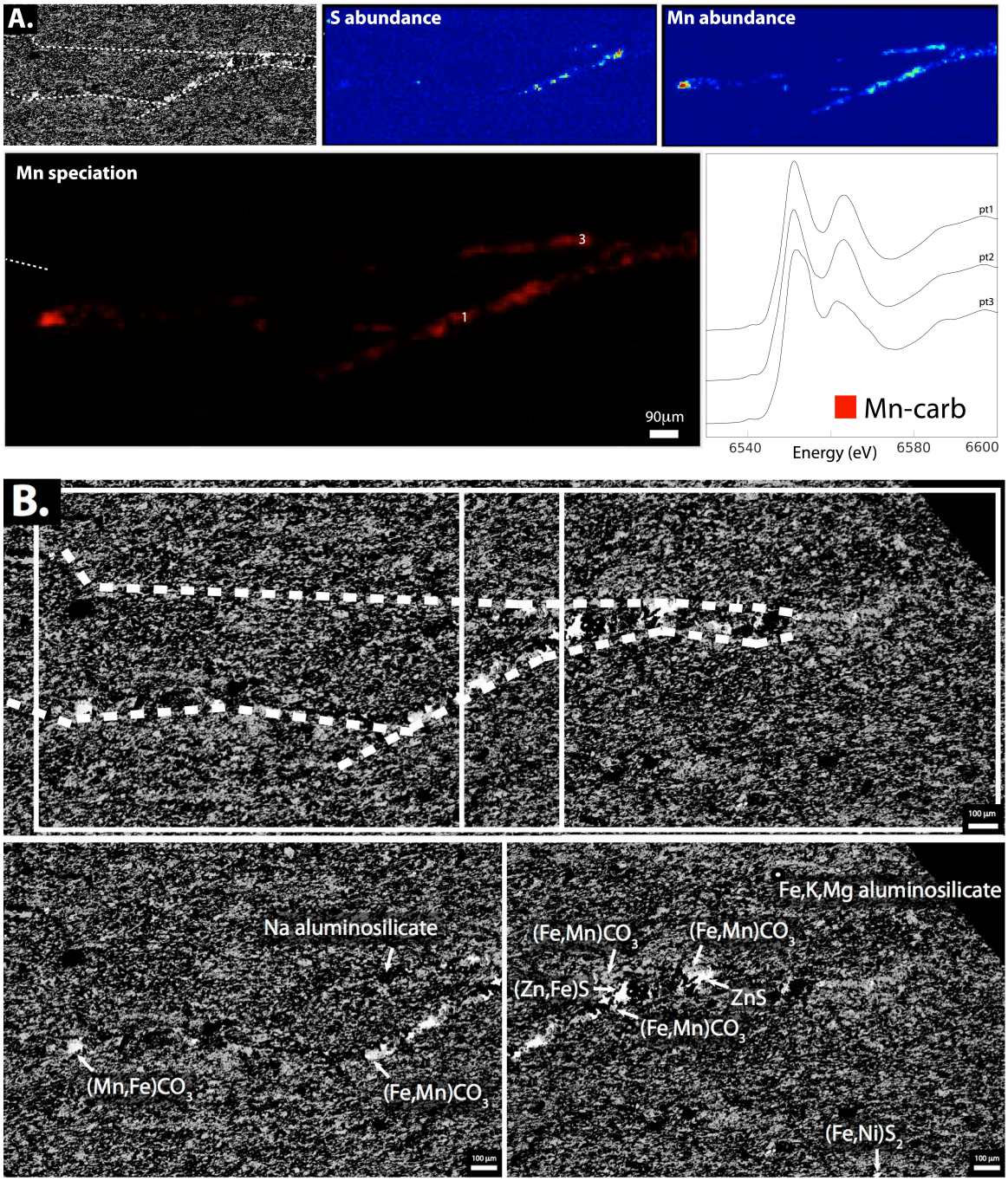

Figure 8 – A. Cross-cutting veins in MF 493m which are enriched in manganese and sulfide phases (see S and Mn X-ray fluorescence maps). Speciation mapping from multiple energy maps of the same region indicates that all manganese is in carbonate. B. Further electron microscopy images and EDS-assisted mineral identifications shown below. Note consistency between Mn-carbonate and sulfide phase locations between SEM and X-ray imaging.

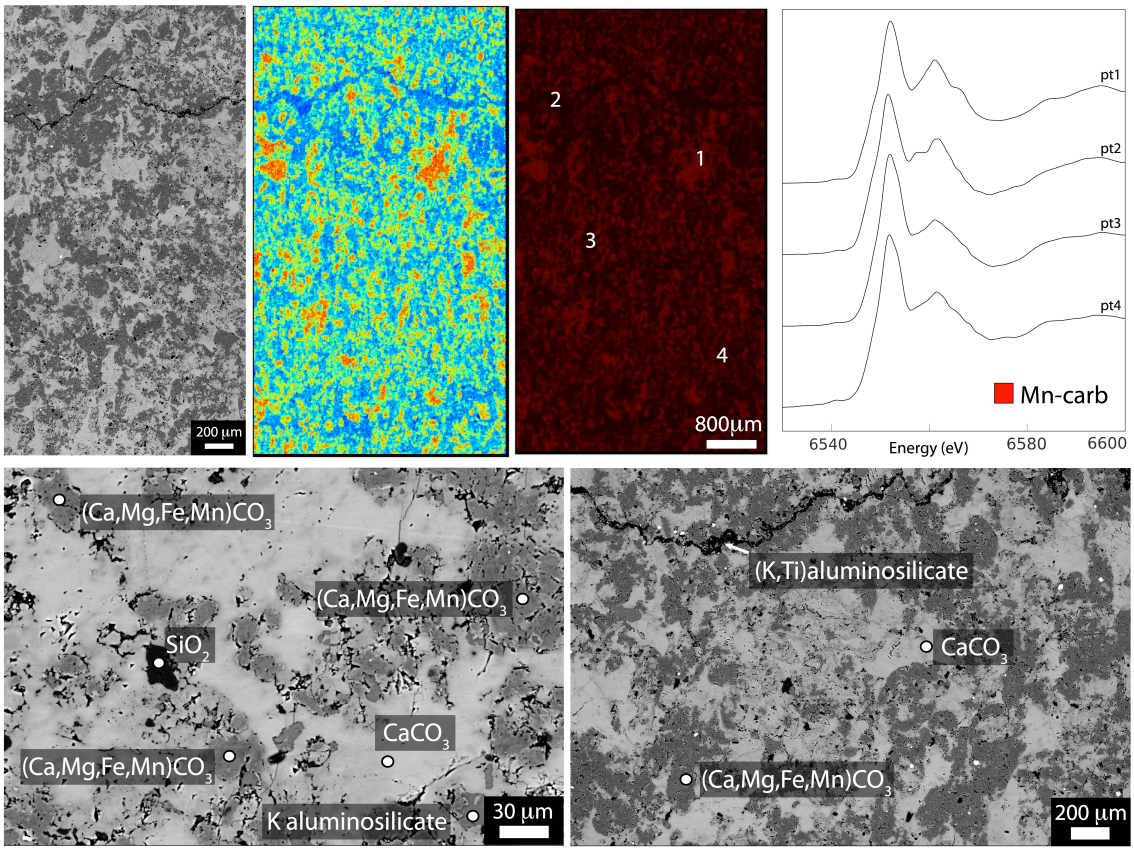

Figure 9 – Representative region from DI 218m, showing heavily recrystallization and incomplete exsolution of calcites and ferrous-magnesian carbonates. All manganese is in low levels in the mixed-cation carbonates and in trace levels in calcites (see Supplementary Table 1). X-ray region shown above with SEM images and identifications shown below.

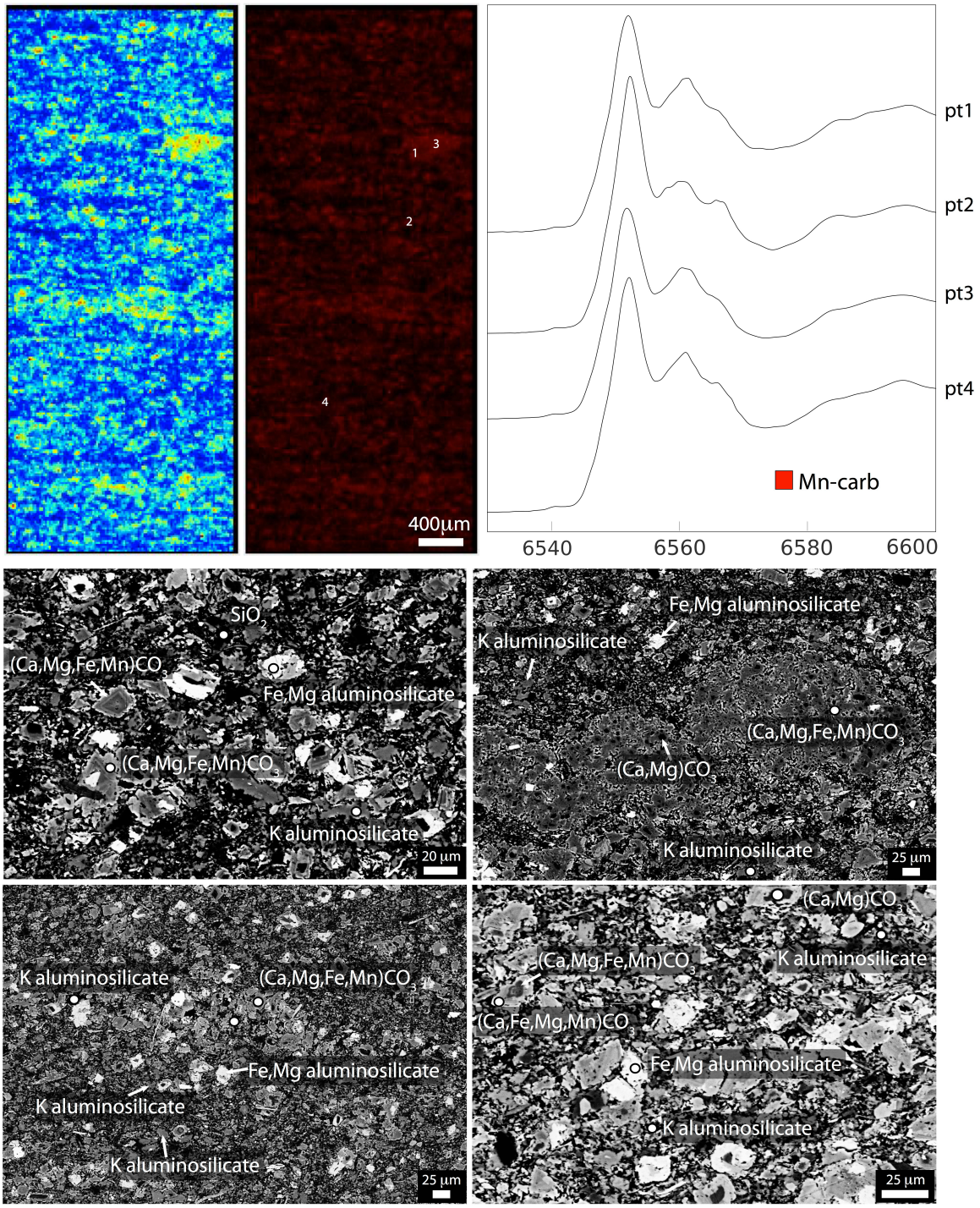

Figure 10 – A representative region from WB 830m, with X-ray spectroscopic imaging and X-ray absorption spectra indicating all manganese is in carbonates. Four SEM image plates of various small-scale textures observed in WB 830 shown below. Carbonates are mainly in euhedral crystals or pore-filling cements, suggesting an early diagenetic origin.

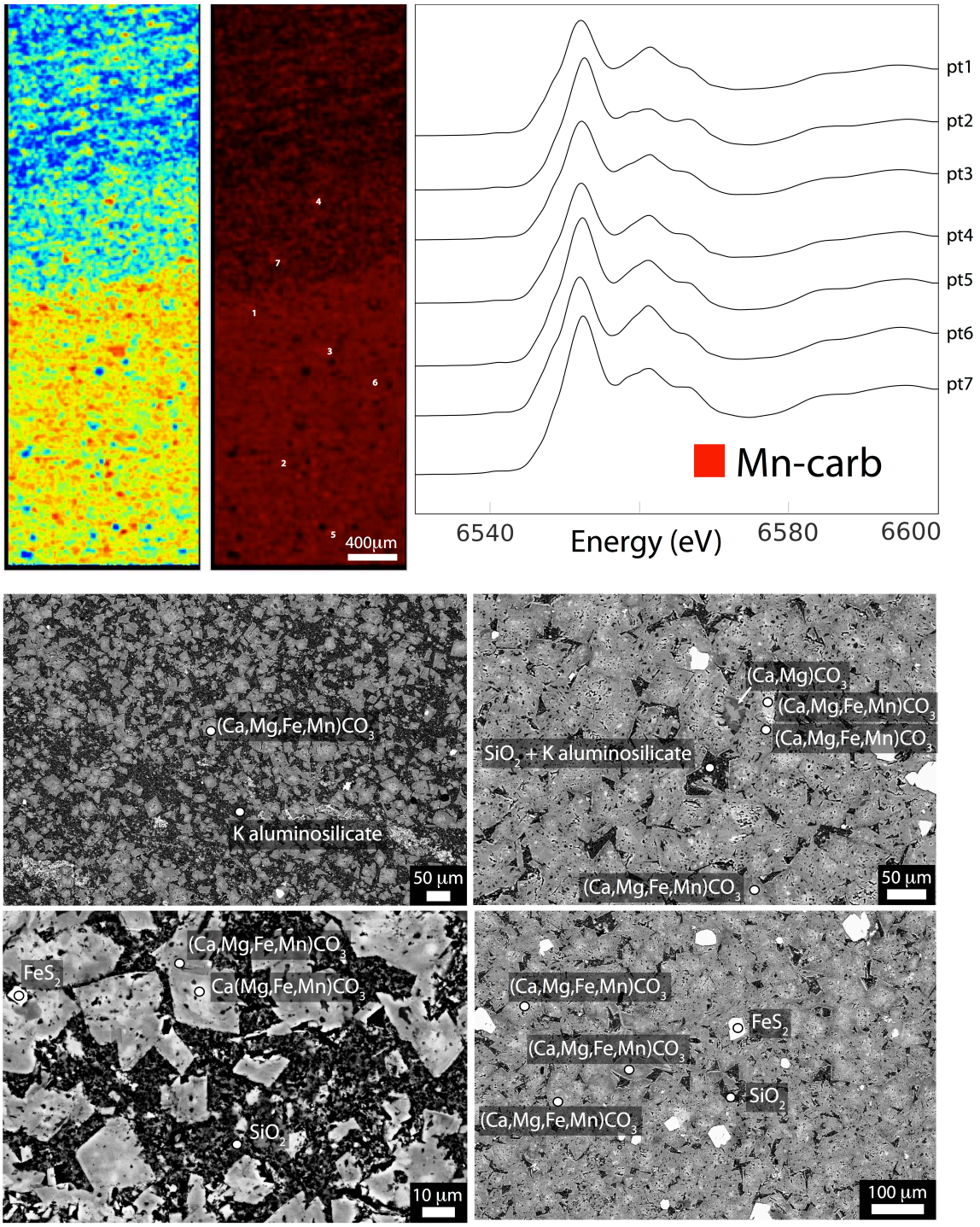

Figure 11 – GKF 338 shown in a representative X-ray spectroscopic image of both the calcium-and-manganese-enriched band and the more clay-rich band. All manganese appears to be in carbonates. SEM images from both regions are shown below, with mineral identifications made using energy dispersive spectrometry (EDS).

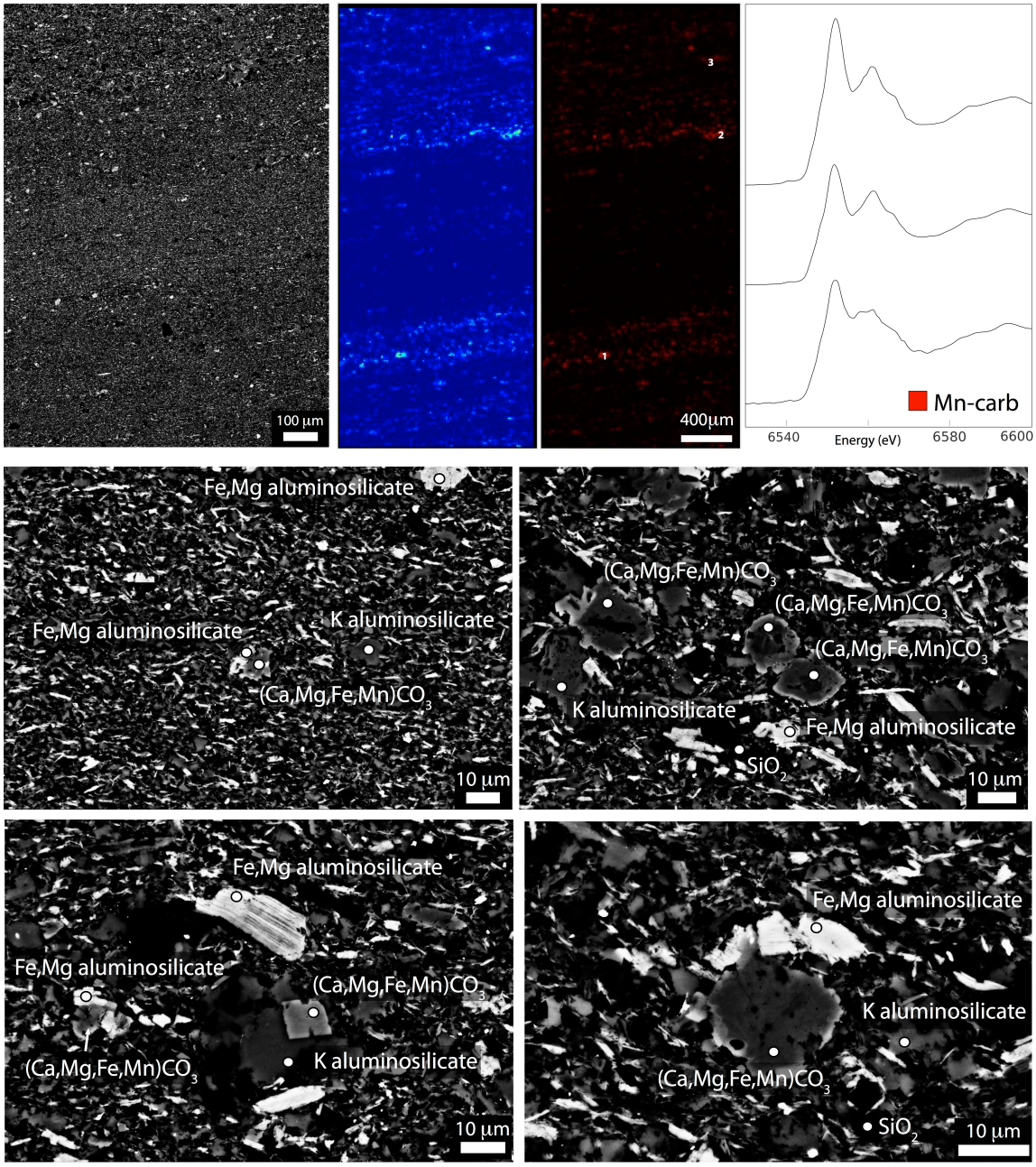

Figure 12 – A representative region of GKP 242, which is dominantly a silica and K-aluminosilicate shale. Coarser bands have more manganese-enriched particles, which are all Mn-bearing carbonates according to X-ray spectroscopic imaging and X-ray absorption spectra. Bottom panels show typical Mn hosts observed on the SEM: all mixed-cation carbonates with low levels of manganese and mainly in rounded carbonate grains, although the image on bottom left is far more euhedral and has higher levels of Fe and Mn.

Table 1 – Whole-rock manganese concentration results from a survey of well-preserved and metamorphosed samples from the Transvaal Supergroup.

Facies	History	MnO (wt. %)	± error
shale	well-preserved	0.348	0.017
shale	well-preserved	0.478	0.024
shale	well-preserved	0.109	0.005
shale	well-preserved	0.086	0.013
shale	well-preserved	0.034	0.005
shale	well-preserved	0.118	0.006
shale	metamorphosed	1.455	0.073
shale	metamorphosed	0.034	0.005
shale	metamorphosed	0.051	0.008
ferruginous shale	metamorphosed	0.173	0.009
ferruginous shale	metamorphosed	0.044	0.007
iron formation (Kur)	well-preserved	0.035	0.005
iron formation (Griq)	well-preserved	0.395	0.020
iron formation (Griq)	well-preserved	0.228	0.011
iron formation (Griq)	well-preserved	0.082	0.012
iron formation (Griq)	well-preserved	0.504	0.025
iron formation (Griq)	well-preserved	0.422	0.021
iron formation (Penge)	metamorphosed	0.684	0.034
iron formation (Penge)	metamorphosed	0.57	0.029
carbonate	well-preserved	0.838	0.042
carbonate	well-preserved	1.005	0.050
carbonate	metamorphosed	0.039	0.006
carbonate	metamorphosed	0.025	0.004

SUPPORTING TABLES

Supporting Table 1 – Point measurements of elemental abundance obtained by energy dispersive spectrometry measurements.

MF402				
carbonates	**Mg**	**Ca**	**Mn**	**Fe**
12	5.66	14.86	0.66	8.4
14	5.93	14.89	0.43	8.68
15	6.1	15.12	0.42	8.6
16	5.13	15.24	0.64	9.08
21	5.72	14.6	0.64	8.55
23	5.52	14.68	1.91	8.19
29	5.23	14.59	1.69	8.42

grunerites	**O**	**Mg**	**Si**	**Mn**	**Fe**
1	59.39	4.78	22.18	0.45	13.14
2	58.98	5.08	21.89	0.42	13.62
7	58.94	5.08	21.86	0.54	13.58
8	59.57	4.75	21.65	0.54	13.48
9	59.06	4.86	22.22	0.48	13.39
19	58.96	5.23	21.84	0.52	13.45
26	58.35	5.07	22.24	0.42	13.91
27	59.23	5	21.72	0.52	13.53
31	59.46	4.98	21.46	0.58	13.28
32	59.03	4.73	21.92	0.51	13.8
35	59.27	4.66	21.65	0.49	13.93

PA2014				
carbonates	**Mg**	**Ca**	**Mn**	**Fe**
2	4.3	16.02	2.36	8.04
7	4.09	17.65	2.65	7.93
65	4.85	16.01	2.43	8.47
66	3.65	16.38	2.67	7.55
67	3.87	16.76	2.52	7.81
68	3.77	16.14	2.5	7.93
58	3.88	13.99	2.2	6.61
32	1.41	21.53	1.74	3.62
33	3.79	15.73	2.5	7.11
59	3.7	16.2	2.41	7.3
60	3.79	16.19	2.52	7.57
61	3.97	16.08	2.5	7.6
62	2.66	18.73	2.15	6.33
63	3.58	15.77	2.42	7.35
64	3.61	15.4	2.41	7.39

grunerite	O	Mg	Si	Mn	Fe
5	54.22	5.14	24.32	1.05	15.27
6	57.85	5.15	21.7	0.9	13.65
8	57.59	4.9	22.45	0.86	13.97
16	58.15	5.06	22.07	0.85	13.44
36	58.03	5	22.19	0.78	13.53
41	58.33	5.23	21.89	0.83	13.51
44	57.6	5.05	21.92	0.82	14.09
46	58.22	4.93	22.06	0.8	13.84
21	58.22	5.01	22.11	0.87	13.78
22	58.64	4.94	21.95	0.88	13.46
26	58.46	5.01	21.78	0.79	13.5
27	57.59	5.15	22.24	1.05	13.97
28	58.41	5.06	22.06	0.89	13.58
30	57.91	5.02	22.08	0.98	13.82
31	57.93	5.05	22.07	0.99	13.72
47	58.16	5.06	22.17	0.83	13.67
54	58.06	5.05	21.99	0.86	13.65
73	58.52	5.02	21.96	0.87	13.53
74	58.56	5.2	21.92	0.76	13.41
75	57.54	4.99	22.59	0.94	13.93
78	58.29	5.06	21.75	0.81	13.52
79	59.45	4.86	21.55	0.72	12.89
80	57.63	5.32	22.56	0.96	13.43
81	58.26	4.99	22	0.73	13.53
82	58.15	5.22	22	0.87	13.6
83	59.44	4.73	18.58	2.97	13.49
84	57.49	5.01	22.19	0.95	14.35
85	60.78	5.07	20.89	0.65	12.1
86	59.54	4.9	21.66	0.74	13.16
87	58.95	5.06	21.53	0.78	13.29

garnet	O	Al	Si	Ca	Mn	Fe
3	56.16	10.69	16.05	2.77	4.98	9.36
18	56.72	10.51	15.82	2.77	4.63	9.22
19	56.44	10.63	16.07	2.82	4.63	9.41
40	56.73	10.42	15.88	2.79	4.92	8.86
43	56.77	10.61	15.89	2.77	4.15	9.82
49	56.46	10.49	15.89	2.8	4.59	9.42
50	57.05	10.77	15.8	2.73	4.65	8.99
51	57.42	10.25	15.81	2.92	4.6	9

PA1470				
grunerite	**O**	**Mg**	**Si**	**Ca**
3	57.74	3.5	22.4	0.12
2	58.72	3.65	22.11	
5	57.96	3.66	22.36	
6	59.07	3.76	21.89	0.07
7	58.11	3.61	22.17	
8	58.05	3.5	22.36	
14	58.25	3.44	22.26	0.07
18	57.59	3.71	22.47	
19	57.25	3.69	22.81	
20	57.9	3.66	22.43	
21	57.9	3.49	22.48	
22	58.45	3.31	21.68	0.12
23	58.17	3.6	22.22	
24	58.22	3.41	22.29	0.06
25	57.75	3.72	22.42	

carbonates	**Mg**	**Ca**	**Mn**	**Fe**
10	0.31	28.09	0.65	1.79
11	2.92	15.96	1.23	9.51
12	2.93	15.84	1.18	9.44
15	3.13	16.11	1.19	9.9
16	3.18	16.1	1.2	10.06
17	3.27	15.66	1.24	9.89

MF 493				
carbonates	**Mg**	**Ca**	**Mn**	**Fe**
53	1.92	1.12	12.49	19.67
54	2.52	0.87	14.27	15.26
56	2.12	1.01	11.76	18.58
57	5.15	0.87	6.05	19
58	1.25	2.51	17.44	12.86

PA 886				
ilmenite	**O**	**Ti**	**Mn**	**Fe**
17	62.09	24.61	1.04	11.83
9	60.17	18.72	0.95	17.09
2	57.34	21.48	1.12	20.06

DI-1					
carbonates	**Mg**	**Ca**	**Mn**	**Fe**	**total**
29	8.29	16.75	0.65	4.18	29.87
30	9.38	15.53	0.54	3.87	29.32
31	10.72	17.68	0.82	4.48	33.7
32	9.21	15.42	0.67	3.78	29.08
33	10.92	16.73	0.64	3.91	32.2
34	0.23	42.84	0.61	0.36	44.04
35		33.69	0.29	0.28	34.26
24	0.19	38.42	0.23	0.31	39.15
25	11.2	17.87	0.71	4.35	34.13
28	10.42	17.33	0.79	4.27	32.81
10	0.34	31.74	0.46	0.35	32.89
11		37.29	0.61	0.37	38.27
12		30.9	0.34	0.37	31.61
13	0.39	33.49	0.44	0.42	34.74
14	10.11	16.53	0.69	4.24	31.57
15	9.42	15.07	0.66	3.91	29.06
16	9.15	15.32	0.63	3.63	28.73
18	9.92	15.8	0.68	3.64	30.04
1	0.27	32.7	0.43	0.38	33.78
2	10.24	16.25	0.67	3.82	30.98
6	9.16	15.8	0.7	3.98	29.64
7	9.78	15.55	0.64	3.42	29.39
8	10.22	15.79	0.53	3.58	30.12

proportionMg	**Ca**	**Mn**	**Fe**	**Temperatures predicted**	
0.277535989	0.56076331	0.02176096	0.13993974		
0.319918145	0.52967258	0.01841746	0.13199181		
0.31810089	0.52462908	0.02433234	0.13293769		
0.316712517	0.53026135	0.02303989	0.12998624		
0.339130435	0.51956522	0.01987578	0.12142857		
0.005222525	0.97275204	0.01385104	0.00817439	**255.1062447**	
0	0.98336252	0.00846468	0.0081728	**[NA]**	
0.004853129	0.98135377	0.00587484	0.00791826	**249.1389068**	
0.328157047	0.52358629	0.02080281	0.12745385		
0.317586102	0.52819262	0.02407802	0.13014325		
0.010337489	0.96503497	0.01398601	0.01064153	**317.9687819**	
0	0.97439247	0.01593938	0.00966815	**[NA]**	
0	0.97753875	0.01075609	0.01170516	**[NA]**	
0.011226252	0.96401842	0.01266552	0.01208981	**326.5897772**	
0.320240735	0.52359835	0.02185619	0.13430472		
0.324156917	0.51858224	0.02271163	0.13454921		
0.318482423	0.53324052	0.0219283	0.12634876		
0.330226365	0.52596538	0.02263648	0.12117177		
0.007992895	0.96802842	0.01272943	0.01124926	**292.6060033**	
0.33053583	0.52453196	0.02162686	0.12330536		
0.309041835	0.53306343	0.02361673	0.134278		
0.332766247	0.52909153	0.02177611	0.11636611		
0.339309429	0.52423639	0.01759628	0.1188579	**average Mg of all calcite**	**Temp predicted**
				0.00495404	**250.79928**

WB 830				
carbonates	Mg	Ca	Mn	Fe
1	6.22	13.8	0.35	3.43
3	9.08	13.36	0.21	2.07
4	5.64	10.83	0.3	3.92
7	11.39	15.09	0.15	0.64
9	6.84	14.97	0.62	2.52
10	8.14	12.55	0.43	2
17	6.51	16.53	0.97	3.15
18	6.62	13.95	0.42	3.17
19	5.26	11.65	0.24	3.04
21	6.03	12.01	0.34	3.14
25	4.7	9.48	0.39	4.15
26	5	10.32	0.53	3.59
27	4.56	8.98	0.45	4
30	4.19	9.51	0.13	2.67
33	4.56	9.01	0.35	4.08
34	4.47	9.24	0.37	4.22
43	9.79	10.9	0.14	0.61
44	4.64	10.57	0.17	3.04
45	6.1	10.03	0.27	2.85
46	5.11	9.11	0.27	3
47	8.23	11.05	0.1	0.38
48	10.38	13.13	0.13	0.19
50	5.66	11.55	0.31	2.49
52	5.93	11.52	0.74	2.39
53	5.84	11.17	0.39	1.71

GKF 338				
carbonates	Mg	Ca	Mn	Fe
61	8.29	15.13	0.63	2.51
62	8.93	24.32	0.62	1.98
69	9.22	18.08	0.75	2.08
70	6.55	10.81	0.73	2.5
71	7.24	11.71	0.67	1.87
74	5.43	9.45	0.73	2.44
72	10.82	12.14	0.46	0.64

73	7.77	13.1	0.52	1.44
74	5.43	9.45	0.73	2.44
75	8.02	13.21	0.48	1.76
76	6.39	10.6	0.42	1.47
77	8.99	11.91	0.4	1.33
88	1.65	24.77	0.7	1.85
89	6.6	9.72	0.41	1.63
79	5.65	9.13	0.54	2.5
80	5.03	7.8	0.5	2.24
81	6.59	9.99	0.41	1.55
86	6.36	11.72	0.65	2.07

GKP 242m					
carbonates	**Mg**	**Ca**	**Mn**	**Fe**	
95	4.99	8.07	0.31	2.98	
103	6.93	12.15	0.49	3.65	
113	5.22	11.17	1.29	4.82	[euhedral crystal]
117	4.64	8.1	0.38	3.6	
130	6.52	11	0.45	3.09	
131	6.49	9.34	0.45	1.99	
132	5.73	9.05	0.42	1.88	
133	5.33	8.91	0.29	2.35	

REFERENCES

Altermann W. and Nelson D. R. (1998) Sedimentation rates, basin analysis and regional correlations of three Neoarchaean and Palaeoproterozoic sub-basins of the Kaapvaal craton as inferred from precise U–Pb zircon ages from volcaniclastic sediments. *Sediment. Geol.* **120**, 225–256.

Beukes N. J. (1987) Facies relations, depositional environments and diagenesis in a major early Proterozoic stromatolitic carbonate platform to basinal sequence, Campbellrand Subgroup, Transvaal Supergroup, Southern Africa. *Sediment. Geol.* **54**, 1–46.

Beukes N. J. (1984) Sedimentology of the Kuruman and Griquatown Iron-formations, Transvaal Supergroup, Griqualand West, South Africa. *Precambrian Res.* **24**, 47–84.

Beukes N. and Klein C. (1992) Models for Iron-Formation Deposition. In *The Proterozoic Biosphere: A Multidisciplinary Study* (eds. J. W. Schopf and C. Klein). Cambridge University Press.

Buick I. S., Maas R. and Gibson R. (2001) Precise U–Pb titanite age constraints on the emplacement of the Bushveld Complex, South Africa. *J. Geol. Soc.* **158**, 3–6.

Burnham C. W. (1979) Magmas and hydrothermal fluids. In *Geochemistry of Hydrothermal Ore Deposits* (ed. H. L. Barnes). John Wiley & Sons, New York. pp. 71–136.

Dyar M. D., Gunter M. E., Delaney J. S., Lanzarotti A. and Sutton S. R. (2002) Systematics in the structure and XANES spectra of pyroenes, amphiboles, and micas as derived from oriented single crystals. *Can. Mineral.* **40**, 1375–1393.

Eriksson P. G., Hattingh P. J. and Altermann W. (1995) An overview of the geology of the Transvaal Sequence and

Bushveld Complex, South Africa. *Miner. Deposita* **30**, 98–111.

Goldsmith J. R. and Newton R. C. (1969) P-T-X relations in the system CaCO3-MgCO3 at high temperatures and pressures. *Am. J. Sci.* **267-A**, 160–190.

Guo Q., Strauss H., Kaufman A. J., Schröder S., Gutzmer J., Wing B., Baker M. A., Bekker A., Jin Q., Kim S.-T. and Farquhar J. (2009) Reconstructing Earth's Surface Oxidation Across the Archean-Proterozoic Transition. *Geology* **37**, 399–402.

Gutzmer J. (1996) Genesis and alteration of the Kalahari and Postmasburg manganese deposits, Griqualand West, South Africa. Rand Afrikaans University.

Harris H. W., El-Naggar M. Y., Bretschger O., Ward M. J., Romine M. F., Obraztsova A. Y. and Nealson K. H. (2010) Electrokinesis is a microbial behavior that requires extracellular electron transport. *Proc. Natl. Acad. Sci.* **107**, 326–331.

Harris N., McMillan A., Holness M., Uken R., Watkeys M., Rogers N. and Fallick A. (2003) Melt generation and fluid flow in the thermal aureole of the Bushveld Complex. *J. Petrol.* **44**, 1031–1054.

Holland H. D. (1984) *The Chemical Evolution of the Atmosphere and Oceans*., Princeton University Press.

Johnson J. E., Gerpheide A., Lamb M. P. and Fischer W. W. (2014) O2 constraints from Paleoproterozoic detrital pyrite and uraninite. *Geol. Soc. Am. Bull.* **126**, 813–830.

Johnson J. E., Webb S. M., Ma C. and Fischer W. W. (in review) Manganese mineralogy and diagenesis in the sedimentary rock record. *Geochim. Cosmochim. Acta*.

Johnson J. E., Webb S. M., Thomas K., Ono S., Kirschvink J. L. and Fischer W. W. (2013) Manganese-oxidizing photosynthesis before the rise of cyanobacteria. *Proc. Natl. Acad. Sci.* **110**, 11238–11243.

Kaneko Y. and Miyano T. (1990) Contact metamorphism of the Bushveld Complex in the northeastern Transvaal, South Africa. *J. Mineral. Petrol. Econ. Geol.* **85**, 66–81.

Kaufman A. J. (1996) Geochemical and mineralogic effects of contact metamorphism on banded iron-formation: an example from the Transvaal Basin, South Africa. *Precambrian Res.* **79**, 171–194.

Kirschvink J. L., Gaidos E. J., Bertani L. E., Beukes N. J., Gutzmer J., Maepa L. N. and Steinberger R. E. (2000) Paleoproterozoic snowball Earth: Extreme climatic and geochemical global change and its biological consequences. *Proc. Natl. Acad. Sci.* **97**, 1400–1405.

Klein C. (1968) Coexisting Amphiboles. *J. Petrol.* **9**, 281–330.

De Kock M. O., Evans D. A. D., Kirschvink J. L., Beukes N. J., Rose E. and Hilburn I. (2009) Paleomagnetism of a Neoarchean-Paleoproterozoic carbonate ramp and carbonate platform succession (Transvaal Supergroup) from surface outcrop and drill core, Griqualand West region, South Africa. *Precambrian Res.* **169**, 80–99.

Komiya T., Hirata T., Kitajima K., Yamamoto S., Shibuya T., Sawaki Y., Ishikawa T., Shu D., Li Y. and Han J. (2008) Evolution of the composition of seawater through geologic time, and its influence on the evolution of life. *Gondwana Res.* **14**, 159–174.

Kontak D. J. and Corey M. (1988) Metasomatic origin of spessartine-rich garnet in the South Mountain Batholith, Nova Scotia. *Can. Mineral.* **26**, 315–334.

Lee C. A. (1996) A Review of Mineralization in the Bushveld Complex and some other Layered Intrusions. In *Developments in Petrology* (ed. R. G. Cawthorn). Layered Intrusions. Elsevier. pp. 103–145. Available at: http://www.sciencedirect.com/science/article/pii/S0167289496800066 [Accessed April 14, 2015].

Luther G. W. I. (2010) The Role of One- and Two-Electron Transfer Reactions in Forming Thermodynamically Unstable Intermediates as Barriers in Multi-Electron Redox Reactions. *Aquat. Geochem.* **16**, 395–420.

Mayhew L. E., Webb S. M. and Templeton A. S. (2011) Microscale imaging and identification of Fe speciation and distribution during fluid-mineral reactions under highly reducing conditions. *Environ. Sci. Technol.* **45**, 4468–4474.

Maynard J. B. (2010) The Chemistry of Manganese Ores through Time: A Signal of Increasing Diversity of Earth-Surface Environments. *Econ. Geol.* **105**, 535–552.

Miyano T. and Beukes N. J. (1997) Mineralogy and Petrology of the Contact Metamorphosed Amphibole Asbestos-bearing Penge Iron Formation, Eastern Transvaal, South Africa. *J. Petrol.* **38**, 651–676.

Miyano T. and Beukes N. J. (1984) Phase relations of stilpnomelane, ferri-annite, and riebeckite in very low-grade metamorphosed iron-formations. *South Afr. J. Geol.* **87**, 111–124.

Okita P. M., Maynard J. B., Spiker E. C. and Force E. R. (1988) Isotopic evidence for organic matter oxidation by manganese

reduction in the formation of stratiform manganese carbonate ore. *Geochim. Cosmochim. Acta* **52**, 2679–2685.

Ollila J. T. (1984) Fluid inclusion and tin deposition at Zaaiplaats, South Africa. *Bull. Geol. Soc. Finl.* **56**, 59–73.

Pickard A. . (2003) SHRIMP U–Pb zircon ages for the Palaeoproterozoic Kuruman Iron Formation, Northern Cape Province, South Africa: evidence for simultaneous BIF deposition on Kaapvaal and Pilbara Cratons. *Precambrian Res.* **125**, 275–315.

Planavsky N. J., Asael D., Hofmann A., Reinhard C. T., Lalonde S. V., Knudsen A., Wang X., Ossa Ossa F., Pecoits E., Smith A. J. B., Beukes N. J., Bekker A., Johnson T. M., Konhauser K. O., Lyons T. W. and Rouxel O. J. (2014) Evidence for oxygenic photosynthesis half a billion years before the Great Oxidation Event. *Nat. Geosci.* **7**, 283–286.

Roy S. (2000) Late Archean initiaion of manganese metallogenesis: its significance and environmental controls. *Ore Geol. Rev.* **17**, 179–198.

Roy S. (2006) Sedimentary manganese metallogenesis in response to the evolution of the Earth system. *Earth-Sci. Rev.* **77**, 273–305.

Schröder S. (2006) Stratigraphic and geochemical framework of the Agouron drill cores, Transvaal Supergroup (Neoarchean-Paleoproterozoic, South Africa). *South Afr. J. Geol.* **109**, 23–54.

Smith A. J. B., Beukes N. J., Gutzmer J. and Cochrane J. M. (2010) Evidence for dissimilatory manganese reduction and availability of free molecular oxygen during deposition of Mesoarchean Witwatersrand-Mozaan strata. *Mineral. Mag.* **74**, A973.

Stumm W. and Morgan J. J. (1996) *Aquatic Chemistry: Chemical Equilibria and Rates in Natural Waters*. 3rd ed., Wiley-Interscience, New York.

Sumner D. Y. and Beukes N. J. (2006) Sequence stratigraphic development of the Neoarchean Transvaal carbonate platform, Kaapvaal Craton, South Africa. **109**, 11–22.

Sumner D. Y. and Bowring S. A. (1996) U-Pb geochronologic constraints on deposition of the Campbellrand Subgroup, Transvaal Supergroup, South Africa. *Precambrian Res.* **79**, 25–35.

Urban H., Stribrny B. and Lippolt H. J. (1992) Iron and manganese deposits of the Urucum District, Mato Grosso do Sul, Brazil. *Econ. Geol.* **87**, 1375–1392.

Varentsov I. M. (1996) *Manganese Ores of Supergene Zone: Geochemistry of Formation*., Kluwer Academic Publishers, Dordrecht, The Netherlands.

Varentsov I. M. and Grasselly G. eds. (1976) *Geology and geochemistry of manganese: proceedings of the 2nd International Symposium on Geology and Geochemistry of Manganese*., International Symposium on Geology and Geochemistry of Manganese, Sydney.

Veizer J. (1978) Secular variations in the composition of sedimentary carbonate rocks, II. Fe, Mn, Ca, Mg, Si and minor constituents. *Precambrian Res.* **6**, 381–413.

Wallmann K., Aloisi G., Haeckel M., Tishchenko P., Pavlova G., Greinert J., Kutterolf S. and Eisenhauer A. (2008) Silicate weathering in anoxic marine sediments. *Geochim. Cosmochim. Acta* **72**, 3067–3090.

Walraven F., Armstrong R. . and Kruger F. . (1990) A chronostratigraphic framework for the north-central Kaapvaal

craton, the Bushveld Complex and the Vredefort structure. *Tectonophysics* **171**, 23–48.